Weierstraß-Institut
für Angewandte Analysis und Stochastik

Leibniz-Institut im Forschungsverbund Berlin e. V.

Preprint ISSN 2198-5855

Design of thin micro-architectured panels with extension-bending coupling effects using topology optimization

Filippo Agnelli [1], Grigor Nika [2], Andrei Constantinescu[1]

submitted: September 3, 2021

[1] LMS, CNRS, École Polytechnique
Institut polytechnique de Paris
91128 Palaiseau
France
E-Mail: filippo.agnelli@polytechnique.edu
andrei.constantinescu@polytechnique.edu

[2] Weierstrass Institute
Mohrenstr. 39
10117 Berlin
Germany
E-Mail: grigor.nika@wias-berlin.de

No. 2873
Berlin 2021

2020 *Mathematics Subject Classification.* 74K20, 74P10, 74P15, 49M41.

Key words and phrases. Topology optimization, micro-architectured panels, shape morphing, inverse homogenization, level set method.

F. A. acknowledges the support of the French doctoral fellowship "Contrat Doctoral Spécifique pour Normalien". G. N. gratefully acknowledges the funding by the Deutsche Forschungsgemeinschaft (DFG, German Research Foundation) under Germany's Excellence Strategy – The Berlin Mathematics Research Center MATH+ (EXC-2046/1, project ID: 390685689) in project AA2-10. The authors are indebted to Charles Dapogny and Bogdan Vernescu for their help and fruitful discussions.

Edited by
Weierstraß-Institut für Angewandte Analysis und Stochastik (WIAS)
Leibniz-Institut im Forschungsverbund Berlin e. V.
Mohrenstraße 39
10117 Berlin
Germany

Fax: +49 30 20372-303
E-Mail: preprint@wias-berlin.de
World Wide Web: http://www.wias-berlin.de/

Design of thin micro-architectured panels with extension-bending coupling effects using topology optimization

Filippo Agnelli, Grigor Nika, Andrei Constantinescu

Abstract

We design thin micro-architectured panels with programmable macroscopic behaviour using inverse homogenization, the Hadamard shape derivative, and a level set method in the diffuse interface context. The optimally designed microstructures take into account the extension-bending effect in addition to in-plane stiffness and out-of-plane bending stiffness. Furthermore, we present numerical examples of optimal microstructures that attain different targets for different volume fractions and interpret the physical significance of the extension-bending coupling. The simultaneous control of the in-plane, out-of-plane and their coupled behaviour enables to shift a flat panel into a dome or saddle shaped structure under the action of an in-plane loading. Moreover, the obtained unit cells are elementary blocks to create three-dimensional objects with shape-morphing capabilities.

1 Introduction

Improved additive manufacturing capabilities have facilitated exploitation of material design to create intricate microarchitectures with macroscopically programmable behaviour. This contemporary advancement of manufacturing technologies has led to the widespread adoption of materials with complex microstructures over the last decades [46, 18, 24, 29, 30, 17, 41, 12, 8]. The attainability of said materials to be constructed through sophisticated, hierarchical microstructures, allows them to avoid inherently conflicting mechanical properties in engineering practice. Hence, it is no surprise that they are highly desirable by engineers and physical scientists.

An example of a material with periodic micro-structure manufactured by classical processes is the honeycomb elastic panel [32, 37]. It has witnessed many applications in industry due to its high strength-to-weight ratio [45, 68] and its exceptional properties outside the elastic domain [62, 69, 43]. In the context of panels, the manufacturing of tailored micro-architecture of the material through various 3D printing technologies opens the way to customize the material distribution through the thickness. The wide range of novel micro-architectures will locally couple various material properties, such as extension and bending response, in what are called generally "transformation mechanisms". The underlying interest is the morphing of flat panels into three-dimensional shells, an ubiquitous mechanism found in nature with increasing technological applications [53].

In engineering, flat panels permitted the development of three-dimensional objects of complex geometries [38, 34, 44] and unleashed new functionalities for exploring harsh or inaccessible environments [56, 40] and delivering increasingly large and complex payloads [12, 22]. However, due to their micro-structural intricacy, panel equations and associated boundary conditions are utilized and applied on a macroscopic scale where often extension–bending effects are present. Designing 3D micro-structures with desired extension–bending effects is one of the aims of this work.

DOI 10.20347/WIAS.PREPRINT.2873 Berlin 2021

One of the methods designed for the analysis of micro-architectured materials is the theory of homogenization [4, 15, 58, 23, 45, 10]. In this theory, the effective material properties of periodic structures are defined by the analysis on a periodic cell and, in turn, these properties depend on the mechanics of constituents and the topology of the periodic structure but are independent of the external boundary conditions and applied forces. Naturally, there exists a large body of work deriving the homogenized equations of panels/plates [20, 39, 42, 45, 57]. For panels with thickness comparable to the length of the period, the derived effective model consists of a coupled system of equations, one equation models the in-plane behaviour of the panel while the second equation models the flexural curvature. Consequently, three sets of effective coefficients are obtained that can be computed numerically once a geometry and volume fraction are determined [20, 42, 45]. The first set of effective coefficients captures the in-plane panel stiffness, the second set captures the bending stiffness, and the third set captures the extension–bending effect of the panel.

When it comes to designing materials with microstructure, modern numerical methods such as shape and topology optimization [28, 14, 7] have become prevalent in this realm, leading to the design of novel complex morphologies. For periodic materials, the overall properties can be studied using homogenization where the effective coefficients computed take into account the bulk material composition as well as the geometry layout [13]. Topology optimization using inverse homogenization exploits this fact in order to systematically identify optimal topologies and volume fractions for two-dimesional [59, 66, 67, 65, 63, 50, 2] and more recently three-dimensional periodic cell [1, 9, 64]. The works cited above, designed optimal microstructures using inverse homogenization in 2D or 3D for elastic or thermo-elastic material. However, the optimal design of panels seems not to have progressed as rapidly. One of the pioneering papers in the design of composite plates is that of [31], where the authors consider the design of extremely rigid clamped square plates. In their analysis, they consider the out-of-plane displacement of the plate without taking into account any extension–bending effects. More recently two–scale topology optimization of composite plates was undertaken in [51]. The authors assumed that, macroscopically, the plate follows the Reissner–Mindlin theory and considered two optimization problems: in-plane optimization of the periodic cell that maximizes the macroscopic stiffness of the composite plate and in-plane optimization of the periodic cell that maximizes the macroscopic displacements at prescribed nodes. To our knowledge no attempt has been made in the literature to optimize the effective coefficients that control in-plane stiffness, out-of-plane bending, and extension–bending coupling at the same time. In contrast, the work in this article is devoted to designing panels with programmable macroscopic behaviour, governed by the Kirchoff–Love model as that is derived from the theory of homogenization in [20, 42, 45]. Building upon our previous work in [2, 3, 50], we use inverse homogenization and a level set method coupled with the Hadamard shape derivative [7, 5] to construct plate elastic moduli within the periodic cell in the context of the diffuse interphase approach (or smoothed interphase approach) [5] that exhibit certain prescribed macroscopic behaviour for a single material and "void". The diffuse interphase approach entails approximating the sharp interphase between material and "void" with a smooth, thin transitional layer of size $2e$, where $e > 0$ is a small number. This is primarily done for mathematical and physical reasons alike. The approach presented here allows for direct control of the extension–bending coefficient in addition to direct control of the in-plane stiffness and the out-of-plane bending stiffness.

The paper is organized as follows. In Section 2 we specify the problem setting and we present the panel's effective equations and the associate effective moduli. Section 3 is devoted to formulating the cost functional, introducing the level set method in the diffuse interface context and the discussion of the volume constraints. Section 4 presents the optimization algorithm and addresses certain algorithmic issues that arise. Section 5 deals with the implementation and discussion of several numerical examples as well as the physical meaning of the extension-bending coupling. A short summary and additional remarks in Section 6 concludes the paper.

Notation. Throughout the paper will make use of Cartesian coordinates and of the following notation:

- Scalars are denoted by italic letters.
- Vectors, second order tensors and fourth order tensors are denoted by bold face italic letters, e.g. $\boldsymbol{u}{=}\{u_i\}_{i=1}^3$, $\boldsymbol{\sigma}{=}\{\sigma_{ij}\}_{i,j=1}^3$ and $\boldsymbol{C}{=}\{C_{ijk\ell}\}_{i,j,k,\ell=1}^3$.
- We adopt the Einstein summation convention, unless otherwise stated, where Latin indices i, j, k range form 1 to 3 and Greek indices α, β, γ range from 1 to 2.
- The average of a quantity over a region, e.g. $\mathcal{D}$, is denoted by $\langle \bullet \rangle_{\mathcal{D}}$ while by $\langle \bullet \mid \bullet \rangle$ we denote the duality product.
- The dot product between two second order tensors $\boldsymbol{A}$ and $\boldsymbol{B}$ is denoted by $\boldsymbol{A}{:}\boldsymbol{B} = \sum_{i,j=1}^{N} A_{ij}\, B_{ji}$ where A_{ij} and B_{ij} are the tensor components.
- The following differential operators will be used:
  - $\boldsymbol{\nabla}\phi$ with components $\phi_{,i}$
  - $\boldsymbol{\nabla}\boldsymbol{u}$ with components $u_{i,j}$
  - $\boldsymbol{\nabla}{\cdot}\boldsymbol{u} = u_{i,i}$
  - $\boldsymbol{\nabla}{\cdot}\boldsymbol{\sigma}$ with components $\sigma_{ij,j}$

2 Setting of the problem

Domain definition. The panel under consideration is occupying a bounded domain $\Omega_h = \omega \times \left]-h/2, h/2\right[\subset \mathbb{R}^3$, characterised by its neutral plane $\omega \subset \mathbb{R}^2$ of characteristic length L, and by its thickness h along the (O, x_3) axis. The domain Ω_h is delimited by a regular boundary Γ, which is decomposed into a lateral boundary $\Gamma^{\text{lat}} = \partial\omega \times \left] -h/2, h/2\right[$, and a top/bottom boundary $\Gamma^{\pm} = \omega \times \{\pm h/2\}$.

The panel's micro-structure is characterized by an in-plane periodic arrangement, composed of a large number of identical unit cells. The period, i.e. the characteristic length of a unit cell ℓ, is assumed to be small in comparison to the characteristic size of the panel L. The small parameter $\epsilon = \mathcal{O}(\ell/L) \ll \mathcal{O}(1)$ referred to as the scale factor, expresses this difference of scales. This scale separation assumption allows one to obtain a set of homogenized plate equations as is presented in the following section. In addition, h and ℓ are assumed to be comparable in scale, for the purposes of this work. Their ratio, denoted by $r = h/\ell = \mathcal{O}(1)$, describes the cell's aspect ratio. This implies that the height is proportional to the small parameter ϵ.

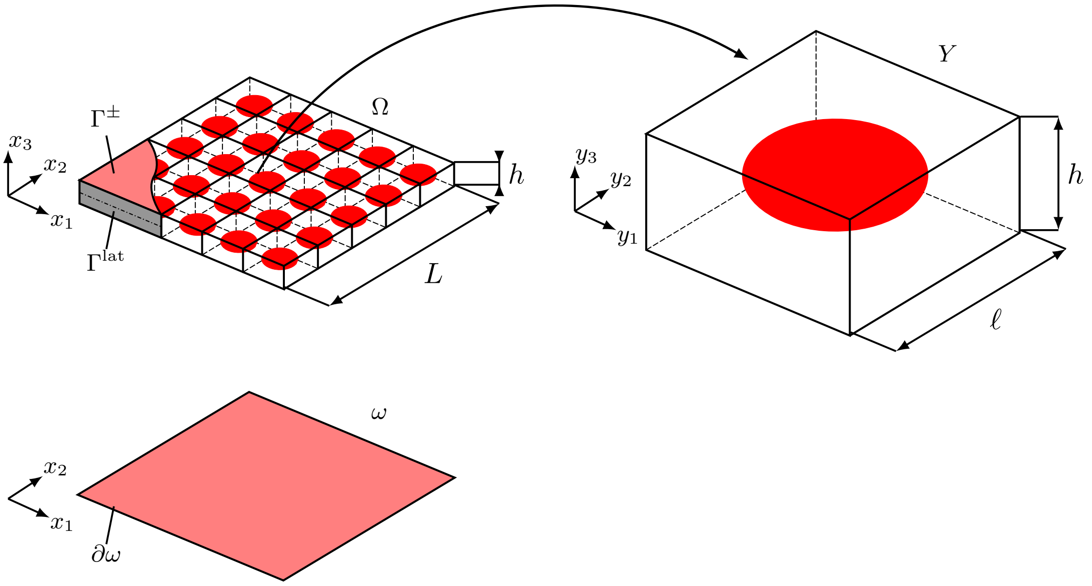

Figure 1: Architectured panel Ω_h with a in-plane periodic arrangement of unit cells Y. The cell's aspect ratio r is defined as $r = h/\ell$. Concept of homogenization yields an equivalent anisotropic homogeneous plate.

Equations at the local scale. Let $Y = [0,1]^2 \times [-r/2, r/2]$ be the rescaled periodic unit cell, described by the set of coordinates $\boldsymbol{y}$ defined as follows:

$$\boldsymbol{y} = \boldsymbol{x}/\epsilon$$

Note that the scaling is made with respect to ϵ for both in-plane and out of the plane components. Through this choice, the rescaled unit cell's Y thus preserves its aspect ratio, unlike in the monograph of Caillerie [20].

The panel is assumed to behave as a linearly elastic anisotropic body. The spatial distribution of the elastic stiffness $\boldsymbol{C}^{\epsilon}$ is expressed by:

$$\boldsymbol{C}^{\epsilon}(\boldsymbol{x}) = \frac{1}{\epsilon^3}\boldsymbol{C}\left(\frac{\boldsymbol{x}}{\epsilon}\right) \tag{1}$$

where $\boldsymbol{C}(\boldsymbol{y})$ is an in-plane periodic, piecewise constant, isotropic fourth order tensor. As proposed by Caillerie in [20], the elastic moduli are assumed to depend on ϵ mainly according to $1/\epsilon^3$: as the plate gets thinner, it becomes stiffer in order to withstand the stresses that are applied to it. Moreover, the solid is submitted to surface traction $\boldsymbol{g}$ at the boundary $\Gamma_{\epsilon}^{\pm}$ and a homogeneous Dirichlet boundary condition for the displacement at the boundary $\Gamma_{\epsilon}^{\text{lat}}$.

In the framework of linear elasticity, the composite panel is governed by the following set of equations

DOI 10.20347/WIAS.PREPRINT.2873

and boundary conditions:

$$\begin{cases} \boldsymbol{\nabla} \cdot \boldsymbol{\sigma}^{\epsilon} = \mathbf{0} & \text{in } \Omega_{\epsilon}, \\ \boldsymbol{\sigma}^{\epsilon} = \boldsymbol{C}^{\epsilon}(\boldsymbol{x}) : \boldsymbol{\varepsilon}(\boldsymbol{u}^{\epsilon}) & \text{in } \Omega_{\epsilon}, \\ \boldsymbol{u}^{\epsilon} = \mathbf{0} & \text{on } \Gamma_{\epsilon}^{\mathrm{lat}}, \\ \boldsymbol{\sigma}^{\epsilon} \cdot \boldsymbol{n} = \boldsymbol{g} & \text{on } \Gamma_{\epsilon}^{\pm}, \end{cases} \tag{2}$$

where $\boldsymbol{u}^{\epsilon}$ is the displacement field, $\boldsymbol{\varepsilon}(\boldsymbol{u}^{\epsilon}) = \frac{1}{2}\left(\boldsymbol{\nabla} \boldsymbol{u}^{\epsilon} + \boldsymbol{\nabla}^{\top} \boldsymbol{u}^{\epsilon}\right)$ is the small strain tensor, and $\boldsymbol{n}$ is the external unit normal of $\Gamma_{\epsilon}^{\pm}$.

Equations at the macroscopic scale. The composite panel is assumed to behave as a linearly elastic anisotropic thin plate. We recall that the plate problem consists in finding a plate displacement field $\boldsymbol{U}(x_1, x_2)$ and the corresponding generalized strain field $(\boldsymbol{\varepsilon}(\boldsymbol{U}), \boldsymbol{\chi}(U_3))$ expressed by:

$$\varepsilon_{\alpha\beta}(\boldsymbol{U}) = \frac{1}{2}\left(U_{\alpha,\beta} + U_{\beta,\alpha}\right), \qquad \chi_{\alpha\beta}(U_3) = -U_{3,\alpha\beta} \tag{3}$$

where $\epsilon_{\alpha\beta}$ is the plane strain, $\chi_{\alpha\beta}$ is the tensor of bending curvature and a generalized stress field $(\boldsymbol{N}, \boldsymbol{M})$ on ω with $\boldsymbol{N}$ the plane stress and $\boldsymbol{M}$ the moments, satisfying the following set of equations (refer to section 8.2. in [57] for further details):

$$\begin{cases} \boldsymbol{\nabla} \cdot \boldsymbol{N} + \boldsymbol{T} = \mathbf{0} & \text{in } \omega \\ \boldsymbol{\nabla} \cdot (\boldsymbol{\nabla} \cdot \boldsymbol{M}) + \boldsymbol{\nabla} \cdot \boldsymbol{Q} - T_3 = 0 & \text{in } \omega \\ \boldsymbol{N} = \boldsymbol{A} : \boldsymbol{\varepsilon}(\boldsymbol{U}) + \boldsymbol{B} : \boldsymbol{\chi}(U_3) & \text{in } \omega \\ \boldsymbol{M} = \boldsymbol{B}^{\top} : \boldsymbol{\varepsilon}(\boldsymbol{U}) + \boldsymbol{D} : \boldsymbol{\chi}(U_3) & \text{in } \omega \\ \boldsymbol{U} = \mathbf{0} & \text{on } \partial\omega \end{cases} \tag{4}$$

where $\boldsymbol{T}$ and $\boldsymbol{Q}$ represent the generalized external loads:

$$\boldsymbol{T} = \int_{\pm h/2} \boldsymbol{g}\, dx_3, \qquad \boldsymbol{Q} = \int_{\pm h/2} x_3\, \boldsymbol{g}\, dx_3,$$

The elastic material behaviour is expressed through the elasticity tensors $\boldsymbol{A}$, $\boldsymbol{B}$ and $\boldsymbol{D}$ with the following symmetries:

$$\begin{aligned} A_{\alpha\beta\gamma\delta} &= A_{\beta\alpha\gamma\delta} = A_{\alpha\beta\delta\gamma} = A_{\gamma\delta\alpha\beta}, \\ B_{\alpha\beta\gamma\delta} &= B_{\beta\alpha\gamma\delta} = B_{\alpha\beta\delta\gamma}, \\ D_{\alpha\beta\gamma\delta} &= D_{\beta\alpha\gamma\delta} = D_{\alpha\beta\delta\gamma} = D_{\gamma\delta\alpha\beta}, \end{aligned}$$

which guarantee symmetry of strains and stresses as well as the existence of an energy potential. In more precise terms, $\boldsymbol{A}$ describes the in-plane behaviour, $\boldsymbol{D}$ describes the bending behaviour, and their coupling is expressed through $\boldsymbol{B}$. Note that in most engineering applications, where panels feature symmetric geometry and material distribution along the thickness, normal and shear behaviour get uncoupled for the membrane part, yielding $\boldsymbol{B} = \mathbf{0}$. The complementary behaviour is investigated here, i.e. we aim at designing panels with exceptional extension-bending coupling effect.

Effective plate moduli. Through periodic homogenization theory we obtain the effective tensors $\boldsymbol{A}^*$, $\boldsymbol{B}^*$ and $\boldsymbol{D}^*$ as first developed by D. Caillerie in [20] (see also [42, 45]). This procedure is schematically depicted in Figure 1. Moreover, the effective thin plate elasticity tensors described above can be computed in their energy form from the solutions of elasticity problems with prescribed mean strain modes. More precisely, the effective coefficients $\boldsymbol{A}^*$, $\boldsymbol{B}^*$ and $\boldsymbol{D}^*$ are expressed, component-wise, as:

$$\begin{aligned}
A^*_{\alpha\beta\gamma\delta} &= \frac{r}{|Y|}\int_Y \Big(\boldsymbol{E}^{\alpha\beta} + \boldsymbol{\varepsilon_y}(\boldsymbol{w}^{\alpha\beta})\Big) : \boldsymbol{C}(\boldsymbol{y}) : \Big(\boldsymbol{E}^{\gamma\delta} + \boldsymbol{\varepsilon_y}(\boldsymbol{w}^{\gamma\delta})\Big)\, d\boldsymbol{y}, \\
B^*_{\alpha\beta\gamma\delta} &= \frac{r}{|Y|}\int_Y \Big(\boldsymbol{X}^{\alpha\beta} + \boldsymbol{\varepsilon_y}(\boldsymbol{p}^{\alpha\beta})\Big) : \boldsymbol{C}(\boldsymbol{y}) : \Big(\boldsymbol{E}^{\gamma\delta} + \boldsymbol{\varepsilon_y}(\boldsymbol{w}^{\gamma\delta})\Big)\, d\boldsymbol{y}, \\
D^*_{\alpha\beta\gamma\delta} &= \frac{r}{|Y|}\int_Y \Big(\boldsymbol{X}^{\alpha\beta} + \boldsymbol{\varepsilon_y}(\boldsymbol{p}^{\alpha\beta})\Big) : \boldsymbol{C}(\boldsymbol{y}) : \Big(\boldsymbol{X}^{\gamma\delta} + \boldsymbol{\varepsilon_y}(\boldsymbol{p}^{\gamma\delta})\Big)\, d\boldsymbol{y}.
\end{aligned} \tag{5}$$

In the above equations, $\boldsymbol{E}^{\alpha\beta}$ (resp. $\boldsymbol{X}^{\alpha\beta}$) are the prescribed mean in-plane (resp. flexural) strain modes on the unit cell, depicted in Figure 2. They are chosen to form a vector basis in the space of second order symmetric tensors and are expressed as:

$$\boldsymbol{E}^{\alpha\beta} = \frac{1}{2}\left(\delta_{i\alpha}\delta_{j\beta} + \delta_{i\beta}\delta_{j\alpha}\right)\boldsymbol{e}_i \otimes \boldsymbol{e}_j, \qquad \boldsymbol{X}^{\alpha\beta} = \frac{y_3}{2}\left(\delta_{i\alpha}\delta_{j\beta} + \delta_{i\beta}\delta_{j\alpha}\right)\boldsymbol{e}_i \otimes \boldsymbol{e}_j, \tag{6}$$

$\boldsymbol{w}^{\alpha\beta}$ and $\boldsymbol{p}^{\alpha\beta}$ are displacement fields, solutions of the 6 local problems (see Figure 2). Let us further remark, that the tensor $\boldsymbol{E}^{\alpha\beta}$ is constant and the tensor $\boldsymbol{X}^{\alpha\beta}$ depends on the vertical position which permits to define the local periodic fields. By introducing the functional space $\mathcal{V}(Y) := \big\{\boldsymbol{v} \in H^1(Y) \mid \boldsymbol{v}$ is (y_1, y_2)-periodic, $\langle v\rangle_Y = 0\big\}$, the cell problems can be expressed in their variational formulation:

$$\begin{aligned}
&\text{Find } \boldsymbol{w}^{\gamma\delta} \in \mathcal{V}(Y) \text{ such that:} \\
&\int_Y \Big(\boldsymbol{E}^{\gamma\delta} + \boldsymbol{\varepsilon_y}(\boldsymbol{w}^{\gamma\delta})\Big) : \boldsymbol{C}(\boldsymbol{y}) : \boldsymbol{\varepsilon_y}(\boldsymbol{\varphi})\, d\boldsymbol{y} = 0, \quad \forall \boldsymbol{\varphi} \in \mathcal{V}(Y).
\end{aligned} \tag{7}$$

$$\begin{aligned}
&\text{Find } \boldsymbol{p}^{\gamma\delta} \in \mathcal{V}(Y) \text{ such that:} \\
&\int_Y \Big(\boldsymbol{X}^{\alpha\beta} + \boldsymbol{\varepsilon_y}(\boldsymbol{p}^{\alpha\beta})\Big) : \boldsymbol{C}(\boldsymbol{y}) : \boldsymbol{\varepsilon_y}(\boldsymbol{\psi})\, d\boldsymbol{y} = 0, \quad \forall \boldsymbol{\psi} \in \mathcal{V}(Y).
\end{aligned} \tag{8}$$

We point out that the first local problem (7) is concerned with the in-plane deformation modes, while the local problem (8) corresponds to the out-of-plane bending modes.

3 Optimization problem

Cost functional. The design domain of the optimization is the periodic cell $Y \in [0,1]^2 \times [-r/2, r/2]$ defined in the previous section. For expediency, we consider only a two-phase material with the extension to multi-phase material being handled as in e.g. [5], [50]. The cell may be decomposed into a strong phase S (typically the material phase), that will also be referred to as *shape*, and weak phase $\bar{S}$ (which represents the void), separated by a interphase ∂S. Moreover, we assume that $(S, \bar{S}) \subset Y$ are smooth, open, bounded subsets and define the set of admissible shapes,

$$\mathcal{U}_{ad} := \{S \subset Y \text{ is open, bounded, and smooth} \mid f_m \leq |S| \leq f_M\} \tag{9}$$

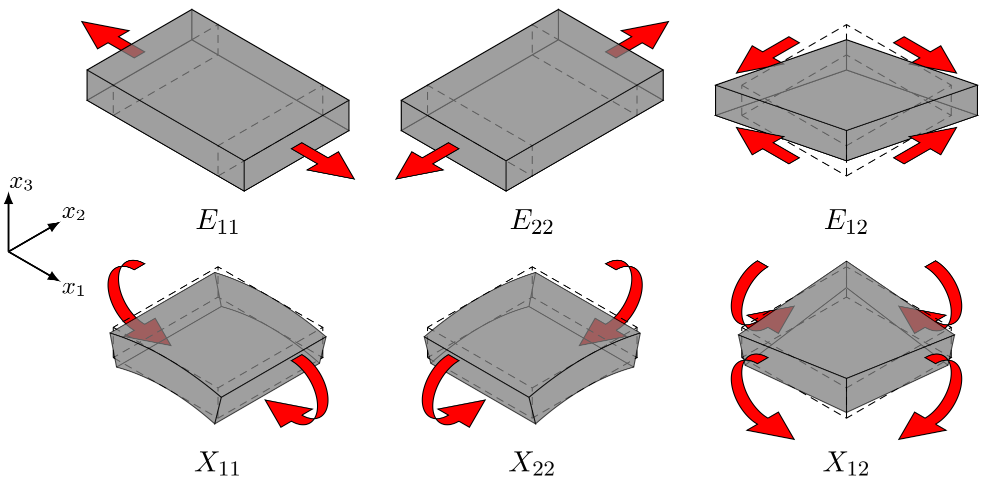

Figure 2: Strain modes imposed to solve the local problems (7) and (8). The undeformed unit cell is represented by dotted lines, whereas the deformed configuration is indicated by solid lines. The first row displays the three in-plane modes, namely two tensions and one in-plane shear, whereas the second row corresponds to the out of the plane modes, namely two bending and one shear bending.

where f_m and f_M are two real numbers ranging between 0 and 1. Hence, we define an objective function $\mathcal{J}$, to be minimized over all possible admissible shapes, as a sum of weighted Euclidean norms:

$$\mathcal{J}(S) = \frac{1}{2}\left\|\boldsymbol{A}^* - \boldsymbol{A}^{\text{target}}\right\|_{\eta_A}^2 + \frac{1}{2}\left\|\boldsymbol{B}^* - \boldsymbol{B}^{\text{target}}\right\|_{\eta_B}^2 + \frac{1}{2}\left\|\boldsymbol{D}^* - \boldsymbol{D}^{\text{target}}\right\|_{\eta_D}^2, \tag{10}$$

where $\boldsymbol{A}^{\text{target}}$, $\boldsymbol{B}^{\text{target}}$ and $\boldsymbol{D}^{\text{target}}$ denote given target thin plate tensor values, while η_A, η_B and η_D are the weight coefficients carrying the same type of symmetry as their respective tensor. Consequently, the topology optimization problem under consideration reads:

$$\begin{gathered}\inf_{S \subset \mathcal{U}_{ad}} \mathcal{J}(S), \\ \text{subject to (7) and (8).}\end{gathered} \tag{11}$$

The constraints are enforced using an augmented Lagrangian method, which is detailed in B. We remark that finding an exact volume fraction compatible with a given elastic stiffness target is a tedious task. Hence, we prefer to choose an interval for the volume fraction rather than setting a specific single value target. The benefit of using an interval volume constraint is two fold: on one hand, if the prescribed material volume fraction is relatively low, the target could fall outside the range of achievable tensors [47, 48], resulting in a final shape with undesired effects (see for example the gap between the target and the obtained results in the two first final shapes of [2]). This is an even bigger issue considering that to our knowledge, variational bounds for elastic thin plates have not yet been studied. On the other hand, if the prescribed material volume fraction is relatively high, the algorithm may converge to shapes that are excessively bulky (e.g. large blocs connected with thin hinges) or in the worst case scenario, it would leave some unconnected material phases (islands) in the final micro-structure.

DOI 10.20347/WIAS.PREPRINT.2873

3.1 Coupling shape sensitivity with a level set description

Shape sensitivity analysis. Shape optimization problems are often not compatible with discrete or zero-order methods [60], rather, they are addressed using gradient-based continuous optimisation algorithms. The notion of gradient for shape optimization problems, namely the method for describing variations of a shape, is based on Hadamard's boundary variation method which has become standard in the literature [55, section 2.6], [26, Chapter 4], [36, Chapter 5], [7, Chapter 6].

Henceforth, the characterization of different phases is described using a level set function and as a consequence, a descent direction can be obtained by computing the shape derivative of $\mathcal{J}(S)$ within the classical shape sensitivity framework of Hadamard. A short description of the level set is provided next, while the detailed derivation of the shape derivative of $\mathcal{J}(S)$ can be found in A for the readers convenience.

Shape representation by the level set method. Developed by Osher and Sethian [54], the level set method is a technique for tracking interfaces which are implicitly defined via the zero level set of an auxiliary scalar function ϕ. The key idea consists in replacing the usual representation of a domain $\omega \subset Y$ by an implicit representation, as the negative sub-domain of an auxiliary scalar function ϕ defined on the whole space Y, as illustrated in Figure 3. More precisely, the shape ω is known via a function $\phi : Y \rightarrow \mathbb{R}$ defined in Equation (12).

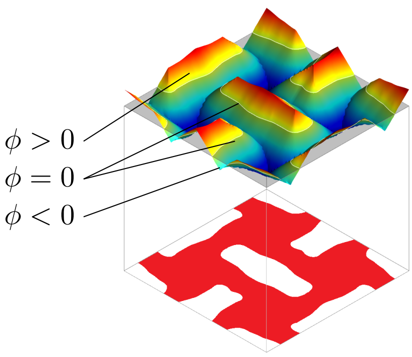

$$\begin{cases} \phi(\boldsymbol{y}) < 0 & \text{if} \quad \boldsymbol{y} \in S & \text{(material)} \\ \phi(\boldsymbol{y}) = 0 & \text{if} \quad \boldsymbol{y} \in \partial S & \text{(boundary)} \\ \phi(\boldsymbol{y}) > 0 & \text{if} \quad \boldsymbol{y} \in \bar{S} = Y \setminus S, & \text{(void)} \end{cases} \tag{12}$$

Figure 3: Representation of the shape in a two-dimensional unit cell: a 3D representation of the level set sliced by the plane $\phi = 0$ projection of the level set on the Cartesian plane (center), characteristic sets defined by the level set, i.e. void and material phases and their reciprocal boundary.

A pseudo time $t \in \mathbb{R}^+$ is defined to characterise the evolution of the shape $S(t)$ via its corresponding level set $\phi(\boldsymbol{y}(t), t)$. Initially the interphase of the shape is described by $\phi(\boldsymbol{y}) = 0$ if $y \in \Gamma^S$. Consequently, for any pseudo time t, $\boldsymbol{y}(t) \in \Gamma^S(t)$ satisfies $\phi(\boldsymbol{y}(t), t) = 0$. Differentiating with respect to the pseudo time t yields:

$$\frac{d\phi}{dt}(\boldsymbol{y}(t), t) = 0 \quad \Rightarrow \quad \frac{\partial \phi}{\partial t}(\boldsymbol{y}, t) + \boldsymbol{\theta}(\boldsymbol{y}, t) \cdot \boldsymbol{\nabla}\phi(\boldsymbol{y}, t) = 0, \tag{13}$$

where $\boldsymbol{\theta} = \frac{\partial \boldsymbol{y}}{dt}$ is the velocity field of the interphase $\Gamma^S(t)$. For a small variation of the shape, its evolution is completely described by the normal component of velocity field $\boldsymbol{\theta}$, as justified by the Hadamard structure theorem [7, 49]. Hence, after introducing the normal component of $\boldsymbol{\theta}$: $V = \boldsymbol{\theta} \cdot \boldsymbol{n}$, eq. (13) can be written as:

$$\frac{\partial \phi}{\partial t}(\boldsymbol{y}, t) + V(\boldsymbol{y}, t)\,|\boldsymbol{\nabla}\phi(\boldsymbol{y}, t)| = 0, \qquad \forall t,\, \forall \boldsymbol{y} \in Y, \tag{14}$$

which takes form of the Hamilton-Jacobi equation.

Smooth interphase approach. In each phase, the material properties are characterised by an isotropic elastic tensor $\boldsymbol{C}^n$ ($n = S$ refers to the stronger phase, $n = \bar{S}$ refer to the weaker one). Assuming a sharp interface would induce a discontinuity of $\boldsymbol{C}^n$. For physical and mathematical reasons it is often desirable to model the interphase as a smooth, transitional layer of thickness $2e$, where e is a small positive parameter. Following the ideas in [5, Section 2], the level set function serves as a base to define the smooth local stiffness tensor $\boldsymbol{C}^e$ in Y as a regular interpolation between the strong phase and the weak phase. The transition from a sharp to a smooth interface is achieved first by redistancing the level set ϕ to become the signed distance function d_S to the interface boundary Γ^S. Then, using a Heaviside type of function we describe the distribution of elastic properties in a smooth way. The Heaviside function $\mathcal{H}_e$ used in this study reads:

$$\mathcal{H}_e(t) = \begin{cases} 0 & \text{if } t < -e, \\ \dfrac{1}{2}\left(1 + \dfrac{t}{e} + \dfrac{1}{\pi}\sin(\dfrac{\pi t}{e})\right) & \text{if } |t| \leq e, \\ 1 & \text{if } t > e. \end{cases} \tag{15}$$

The choice of the regularizing function $\mathcal{H}_e$ is not unique: it is possible to use other type of regularizing functions (see [66] for instance). Hence, the properties of the material occupying the unit cell Y are then defined as a smooth interpolation between the tensors $\boldsymbol{C}^S$ and $\boldsymbol{C}^{\bar{S}}$,

$$\boldsymbol{C}^e = \mathcal{H}_e(d_S)(\boldsymbol{C}^{\bar{S}} - \boldsymbol{C}^S) + \boldsymbol{C}^S, \tag{16}$$

and the material volume fraction $|S|$ is defined by,

$$|S| = \frac{1}{|Y|}\int_Y (1 - \mathcal{H}_e)\, d\boldsymbol{y}. \tag{17}$$

Lastly, from the computations in Appendix A, the expressions for the shape derivative of $\mathcal{J}(S)$ in direction of the velocity field $\boldsymbol{\theta}$ under the approximation of thin smooth interphase reads:

$$\mathcal{J}'(S)(\boldsymbol{\theta}) = -\int_{\Gamma^S} \left(f_A(\boldsymbol{s}) + f_B(\boldsymbol{s}) + f_D(\boldsymbol{s})\right)\, \boldsymbol{\theta}\cdot\boldsymbol{n}\, d\boldsymbol{s}, \tag{18}$$

where

$$\begin{aligned}
f_A(\boldsymbol{s}) &= \frac{r}{|Y|}\left\|\boldsymbol{A}^*(d_S) - \boldsymbol{A}^{\text{target}}\right\|_{\eta_A} \left(\boldsymbol{E}^{\gamma\delta} + \boldsymbol{\varepsilon}_{\boldsymbol{y}}(\boldsymbol{w}^{\gamma\delta})\right) : \left(\boldsymbol{C}^{\bar{S}} - \boldsymbol{C}^S\right) : \left(\boldsymbol{E}^{\alpha\beta} + \boldsymbol{\varepsilon}_{\boldsymbol{y}}(\boldsymbol{w}^{\alpha\beta})\right), \\
f_B(\boldsymbol{s}) &= \frac{r}{|Y|}\left\|\boldsymbol{B}^*(d_S) - \boldsymbol{B}^{\text{target}}\right\|_{\eta_B} \left(\boldsymbol{E}^{\gamma\delta} + \boldsymbol{\varepsilon}_{\boldsymbol{y}}(\boldsymbol{w}^{\gamma\delta})\right) : \left(\boldsymbol{C}^{\bar{S}} - \boldsymbol{C}^S\right) : \left(\boldsymbol{X}^{\alpha\beta} + \boldsymbol{\varepsilon}_{\boldsymbol{y}}(\boldsymbol{p}^{\alpha\beta})\right), \\
f_D(\boldsymbol{s}) &= \frac{r}{|Y|}\left\|\boldsymbol{D}^*(d_S) - \boldsymbol{D}^{\text{target}}\right\|_{\eta_D} \left(\boldsymbol{X}^{\gamma\delta} + \boldsymbol{\varepsilon}_{\boldsymbol{y}}(\boldsymbol{p}^{\gamma\delta})\right) : \left(\boldsymbol{C}^{\bar{S}} - \boldsymbol{C}^S\right) : \left(\boldsymbol{X}^{\alpha\beta} + \boldsymbol{\varepsilon}_{\boldsymbol{y}}(\boldsymbol{p}^{\alpha\beta})\right).
\end{aligned}$$

Hence, a descent direction can always be selected by choosing $\boldsymbol{\theta} = (f_A(\boldsymbol{s}) + f_B(\boldsymbol{s}) + f_D(\boldsymbol{s}))\,\boldsymbol{n}$.

As a final comment, we remark that the smooth interface approach affects any numerical integration and its associated discretization scheme used in all problems.

3.2 Volume constraint

The result in Equation (18) corresponds to the unconstrained problem. To ensure that $S \subset \mathcal{U}_{\text{ad}}$, we rely on an augmented Lagrangian approach to enforce a two-sided inequality constraints [16], [52, Chapter 17]. Hence, the optimisation problem (11) is a constraint-free minimization of a (Lagrangian-like) weighted sum of the cost functional $\mathcal{J}(S)$ and the constraint $\mathcal{P}(S)$ that reads:

$$\begin{aligned} &\inf \Big(\mathcal{J}(S) + \mathcal{P}(S)\Big), \\ &\mathcal{P}(S)[\lambda, \mu] := \min_{f_m \le |S| - \upsilon \le f_M} \left(\lambda\, \upsilon + \frac{\mu}{2}|\upsilon|^2\right), \end{aligned} \tag{19}$$

where λ and μ are the Lagrange multipliers for the volume constraint. A brief presentation on used schemes to update these parameters through the optimisation process is provided in B. From the constraint gives rise to an additional term in the shape derivative of $\mathcal{J}(S)$. We denote by $\mathcal{P}'(S)$ the shape derivative of the volume constraint $\mathcal{P}(S)$ in the direction $\boldsymbol{\theta}$. Under the approximation of thin smooth inter-phase, this reads (see B):

$$\mathcal{P}'(S)(\boldsymbol{\theta}) = -\int_{\Gamma^S} f_P(\boldsymbol{s})\, \boldsymbol{\theta} \cdot \boldsymbol{n}\, d\boldsymbol{s}, \tag{20}$$

where

$$f_P(\boldsymbol{s}) = \begin{cases} \lambda^k + (|S| - f_M)\, \mu^k & \text{if } \lambda^k + \mu^k\,(|S| - f_M) > 0, \\ \lambda^k + (|S| - f_m)\, \mu^k & \text{if } \lambda^k + \mu^k\,(|S| - f_m) < 0, \\ \mathbf{0} & \text{otherwise.} \end{cases}$$

We remark that the above expression has the same form of eq. (18), which means that a descent direction can be found in similar manners.

3.3 Extension and regularization of the velocity field and descent direction

Although eq. (14) for the advection of the level set function is solved in the whole domain Y, shape sensitivity analysis provides us with a shape gradient defined only on the boundary of the domain Γ^S. Since the boundary is not explicitly discretised in our case, we can assume that the normal velocity V is defined for the nodes of the elements that are crossed by the zero level set. Then, one possibility is to consider $V = 0$, $\forall \boldsymbol{y} \in Y \backslash \Gamma^S$. Unfortunately, this choice would limit the movement of the boundary to small distance, which would result in an increased number of iterations until convergence, and thus a slower algorithm. A remedy to this inconvenience is to extend the velocity field in all the domain. At the same time, it would be numerically beneficial to smooth a bit the shape gradient, but in a way that guarantees the descent nature of the new advection velocity. The sequel describes one way to combine these two requirements. Initially, the shape derivative has the form:

$$\mathcal{J}'(S)(\boldsymbol{\theta}) = \sum \int_{\Gamma^S} -\boldsymbol{\theta} \cdot \boldsymbol{n}\, f(\boldsymbol{s})\, d\boldsymbol{s} \tag{21}$$

or, for an advection velocity of the type $\boldsymbol{\theta}(\boldsymbol{s}) = V(\boldsymbol{s})\, \boldsymbol{n}(\boldsymbol{s})$,

$$\mathcal{J}'(S)(V\boldsymbol{n}) = \sum \int_{\Gamma^S} -V(\boldsymbol{s})\, f(\boldsymbol{s})\, d\boldsymbol{s} \tag{22}$$

Instead of choosing $V(\boldsymbol{s}) = -f(\boldsymbol{s})$, we can solve the variational formulation for $Q \in H^1(Y)$:

$$\int_Y \left(\alpha^2\, \boldsymbol{\nabla} Q \cdot \boldsymbol{\nabla} W + W\, Q\right) d\boldsymbol{y} = \mathcal{J}'(S)(W\boldsymbol{n}) \qquad \forall W \in H^1(Y) \tag{23}$$

where $\alpha > 0$ is a positive scalar (of the order of the mesh size) to control the regularization width and take $V = -Q$. This operation reveals that:

$$\mathcal{J}'(S)(V\boldsymbol{n}) = -\int_Y \left(\alpha^2 |\boldsymbol{\nabla} Q|^2 + Q^2\right) d\boldsymbol{y} \tag{24}$$

which guarantees again a descent direction for $\mathcal{J}$.

4 Optimization algorithm

The numerical algorithm used is adapted from [6] accounting for the additional local problem that is needed to compute the effective coefficients of the composite panel.

Data: Initialize a level set function ϕ_0 corresponding to an initial shape S^0;
for $k \geq 0$ *iterate until convergence* **do**

a. Redistance ϕ_k into a signed distance function d_{S^k} for stability reasons;
b. Calculate the local solutions $\boldsymbol{w}^{m\ell}$, $\boldsymbol{p}^{m\ell}$ for $m, \ell = 1, 2$ by solving (7), (8);
c. Deform the domain S^k by solving the Hamilton-Jacobi equation (14);
   - Shape S^{k+1} is characterized by the level set ϕ_{k+1} after a time step Δt_k;
   - The time step Δt_k is chosen so that $\mathcal{J}(S^{k+1}) \leq \mathcal{J}(S^k)$;

end

Algorithm 1: Major steps of the algorithm in [6] adapted to thin composite panels.

Algorithmic issues As we already mentioned in the previous section, it is well known that problems of designing optimal microstructures do not possess a global minimum [7]. As a result initial starting shapes/guesses have a considerable effect on the final design of the micro-structure. If an initial guess does not result in a shape then we can restart the algorithm with the previous guess being our initial guess. Additionally, we can start the algorithm with an initial shape that is a known local minimum from the literature, in which case the algorithm converges very fast.

In order to discuss the influence of the initial design of the material cell on the optimized solution, six kinds of initial designs displayed in Figure 4 were tested. Initial designs can be a straight or diagonal patterns with various micro-perforations. The initial design (a) and (b) feature cylinder inclusions, (c) and (d) feature cone inclusions, (e) and (f) feature circular inclusions. The number and the size of micro-perforations can be varied to tune the initial volume fraction.

We also draw the reader's attention to the conflict between the Hadamard's method for shape variations which supposes that the topology of the shape remains the same, while the level set method lets such changes occur in a natural way. This may result in an increase of the objective function $\mathcal{J}$. As a

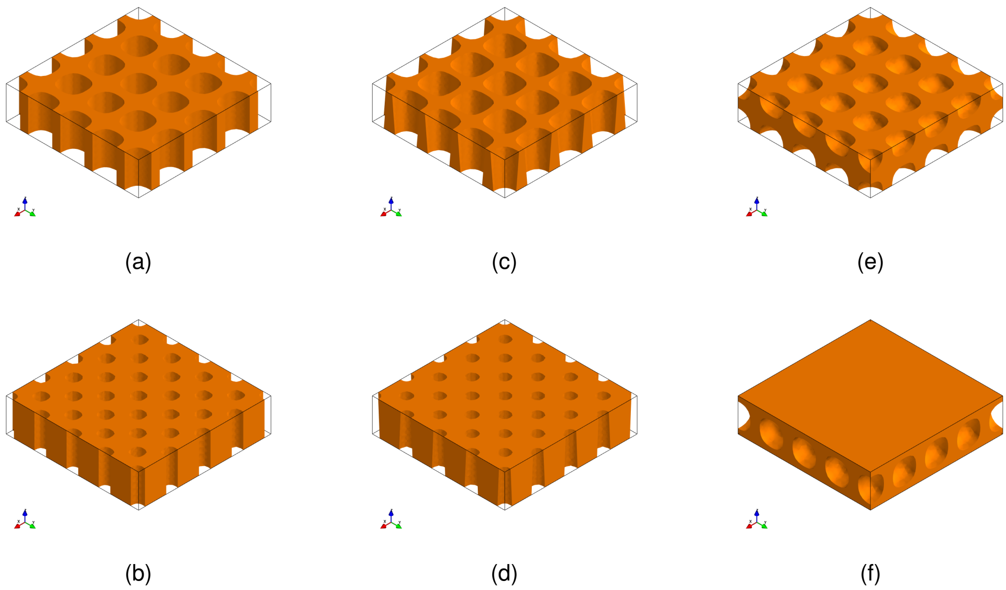

Figure 4: Initial shapes. (a) Square pattern of cylindrical micro-perforations. (b) Diagonal pattern of cylindrical micro-perforations. (c) Square pattern of conic micro-perforations. (d) Diagonal pattern of conic micro-perforations. (e) Straight bubble pattern. (f) Diagonal bubble pattern.

consequence, for the first iterations where most of the topological changes occur, descent steps will be accepted even when the objective function $\mathcal{J}$ will be relaxed up to a tolerance defined as follows:

$$\mathcal{J}(S^{k+1}) < \mathcal{J}(S^k)(1 + \eta_{\text{tol}} \exp(-k)) \tag{25}$$

5 Numerical results

In the following examples, the unit cell Y is a rectangular box of dimensions $1 \times 1 \times 0.25$ (hence the aspect ratio of the length scale $r = 1/4$), meshed with a structured symmetric grid of $50 \times 50 \times 12$ linear tetrahedron elements. We recall that the distribution of elastic properties are defined by eq. (16). The material properties in each phases, S and $\bar{S}$ are characterized by an isotropic fourth order tensor:

$$\boldsymbol{C}^n = \frac{E^n}{1+\nu^n}\boldsymbol{I}_4 + \frac{E^n\,\nu^n}{(1+\nu^n)(1-2\nu^n)}\boldsymbol{I}_2 \otimes \boldsymbol{I}_2 \qquad n \in \{S, \bar{S}\}$$

where $\boldsymbol{I}_2$ is a second order identity matrix, and $\boldsymbol{I}_4$ is the identity fourth order tensor acting on symmetric matrices. The material properties are normalized as follows: the Young's modulus E was set to $E^S = 0.91\,\text{MPa}$ for the strong phase (material) and $E^{\bar{S}} = 0.91 \times 10^{-4}\,\text{MPa}$ for the weak phase (ersatz). The Poisson's ratio was set to $\nu = 0.3$ for both phases. A homogeneous plate made of material $\boldsymbol{C}^S$ (resp. $\boldsymbol{C}^{\bar{S}}$) features an effective in-plane behaviour $A^*_{1111} = A^*_{2222} = r$ (resp. $A^*_{1111} = A^*_{2222} = 10^{-4}r$).

All computations were carried out using an in house coupling of a series of free software. The elasticity problems (7) and (8) are solved using the finite element solver `Cast3M`. The Hamilton-Jacobi equation

(14) is solved using the method of characteristics using the `advect` package developed in [19]. The re-distancing of the level set is undertaken using the `mshdist` package developed in [25]. The optimisation is assumed to be terminated when 200 iterative steps are reached, or else, when the time step in the Hamilton-Jacobi equations becomes too small (the code reached a local minimum and cannot find a descent direction).

Setting the target stiffness. The simultaneous in-plane, out-of-plane and their coupled behaviour permits to program an out-of-plane response that results in either a dome shaped structure or a saddle shaped structure under the action of in-plane loading. As the primary interest in this work is the stretching-bending response of the panels, all shear coefficients, namely A^*_{1212}, B^*_{1212} and D^*_{1212} were left free and are denoted by a star, the controlled coefficients are therefore:

$$\boldsymbol{C}^{\text{target}} = \left[\begin{array}{ccc|ccc} A^*_{1111} & A^*_{1122} & \star & B^*_{1111} & B^*_{1122} & \star \\ A^*_{1122} & A^*_{2222} & \star & B^*_{2211} & B^*_{2222} & \star \\ \star & \star & \star & \star & \star & \star \\ \hline B^*_{1111} & B^*_{2211} & \star & D^*_{1111} & D^*_{1122} & \star \\ B^*_{1122} & B^*_{2222} & \star & D^*_{1122} & D^*_{2222} & \star \\ \star & \star & \star & \star & \star & \star \end{array}\right]. \tag{26}$$

Moreover, by methodically tuning the weights of the cost functional (10) permits to prioritize certain crucial components at the expense of others. Furthermore, all numerical examples reported in the sequel target an elastic tensor exhibiting “quadratic symmetry”, i.e. $A_{1111} = A_{2222}$ and $D_{1111} = D_{2222}$. This simplification, albeit fundamental, demonstrates the capability of the code to discriminate local solutions with general orthotropic behaviour. Additionally, we point out that the values of the coefficients in $\boldsymbol{A}$ are usually much larger than the ones in $\boldsymbol{B}$ and $\boldsymbol{D}$. The difference in scale must be corrected through the weights η_A, η_B and η_D, otherwise if $\mathcal{O}(\eta_A) = \mathcal{O}(\eta_B) = \mathcal{O}(\eta_D)$, the cost functional $\mathcal{J}(S)$ in (10) can be approximated during the first iterations:

$$\mathcal{J}(S) \approx \frac{1}{2} \left\| \boldsymbol{A}^* - \boldsymbol{A}^{\text{target}} \right\|^2_{\eta_A}$$

and, therefore, the algorithm essentially satisfies the prescribed in plane behaviour $\boldsymbol{A}^{\text{target}}$ neglecting $\boldsymbol{B}^{\text{target}}$ and $\boldsymbol{D}^{\text{target}}$. Our experiences concluded that an optimal choice for the weights is: $10^2\, \mathcal{O}(\eta_A) = \mathcal{O}(\eta_B) = \mathcal{O}(\eta_D)$.

A rectangular macroscopic plate is modelled in the finite element solver `Cast3M`. It is meshed with 80×60 discrete Kirchhoff triangular (DKT) shell elements [11, 61]. The constitutive matrix obtained from the optimization is directly included in the calculation. The calculations are conducted with symmetry boundary conditions on the bottom and left side of the plate. The right part is loaded in displacement along the direction $\boldsymbol{e}_1$, yet all the other components and rotations are left free. Rigid body movements are eliminated by fixing the displacements and rotations on a node at the bottom left corner.

5.1 Example 1

The targets of the first micro-structure to be optimized are given in Table 1. To ensure the desired quadratic symmetry, a symmetry of the shape was enforced along both the Ox and Oy axis, by symmetrizing the level set function during the algorithmic iterations. Additionally, the material volume fraction

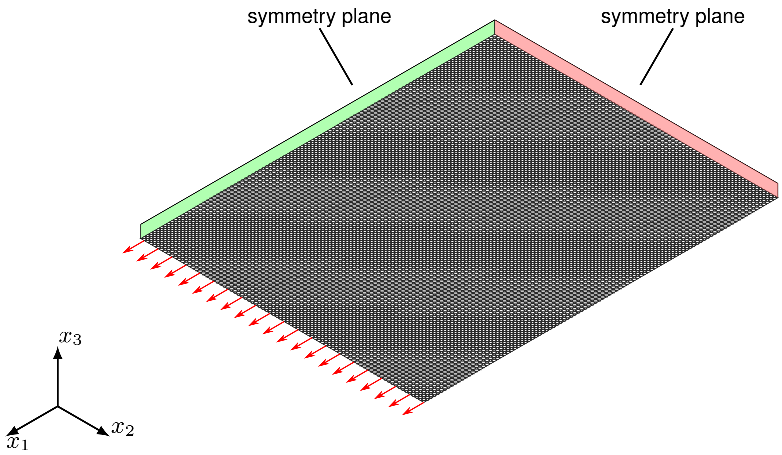

Figure 5: Finite element mesh and boundary conditions for the tensile loading. The amplitude of the imposed displacement is normalized at 0.1 macroscopic strain. The response to other loading can be easily recovered, since it is proportional to the loading at small strain.

was constrained to be between $0.3 \leq |S| \leq 0.5$. The initial shape, depicted in Figure 4(a), is consisting of a square pattern of "cylindrical" micro-perforations. The collected values of all the coefficients of the aforementioned shape are included succinctly in Table 1.

$$
\boldsymbol{C}^{\text{target}} = \left[\begin{array}{ccc|ccc}
0.12 & -0.06 & 0 & \star & 2.3\text{e}^{-3} & 0 \\
-0.06 & 0.12 & 0 & 2.3\text{e}^{-3} & \star & 0 \\
0 & 0. & \star & 0 & 0. & \star \\
\hline
\star & 2.3\text{e}^{-3} & 0 & 6.3\text{e}^{-4} & \star & 0 \\
2.3\text{e}^{-3} & \star & 0 & \star & 6.3\text{e}^{-4} & 0 \\
0 & 0 & \star & 0 & 0 & \star
\end{array}\right]
\qquad
\boldsymbol{C}^{*} = \left[\begin{array}{ccc|ccc}
0.120 & -0.059 & 0 & -1.5\text{e}^{-3} & 1.8\text{e}^{-3} & 0 \\
-0.059 & 0.119 & 0 & 1.7\text{e}^{-3} & 1.0\text{e}^{-4} & 0 \\
0. & 0. & \star & 0. & 0. & \star \\
\hline
\star & 1.7\text{e}^{-3} & 0 & 6.1\text{e}^{-4} & \star & 0 \\
1.8\text{e}^{-3} & \star & 0 & \star & 6.1\text{e}^{-4} & 0 \\
0. & 0. & \star & 0. & 0. & \star
\end{array}\right]
$$

Table 1: Values of the target stiffness tensors and the homogenized tensors for the final form of the micro-structure in Figure 7. Only the entries that have numerical values were controlled. The remaining entries were left free.

The convergence history of the cost functional and of the volume constraint displayed in Figure 6(a) shows that the target coefficient got stabilized in slightly more than 40 iterations and that the later iteration contributed only to small improvements without bringing the cost functional to less than 2×10^{-4}. The evolution of material volume fraction displayed in Figure 6(b) features an initial steep decrease down to 0.25, attributed to the initial swelling of the holes, followed by a slower evolution to up to 0.5, which is the upper limit of the proposed range of the constraint.

The final shape features are in-plane behaviour with an effective Poisson's ratio of -0.5 and a significant value for B_{1122} and B_{2211}, which come close to the target values. In addition, it is worth noticing that the diagonal coefficient in the Oy direction is much smaller than the coefficient in the Ox direction. This implies that when the panel is loaded in the direction Ox, it will exhibit a positive Gaussian curvature, i.e. the panel will morph into a dome shaped structure. Conversely, when the panel is loaded in the direction Oy, the deformed shape will morph into a cylinder (hence a Gaussian curvature close to 0).

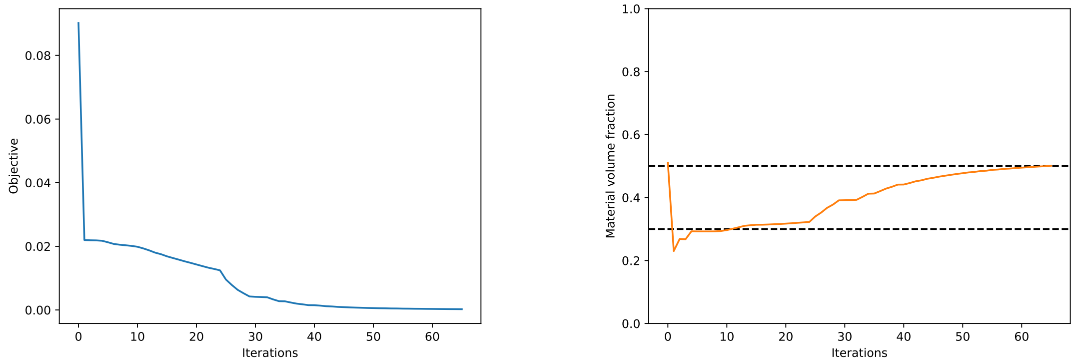

(a) (b)

Figure 6: Evolution of the cost functional (a) and the volume constraint (b) with the number of iterations for the microstructure depicted in Figure 7. After 40 iterations we seem to have rather stable convergence both for the cost functional and volume constraint. The algorithm stops after 65 iterations, because the time step in the advection equation becomes too small.

5.2 Example 2

The targets of the second microstructure to be optimized are given in Table 2. To ensure the desired quadratic symmetry the level set function was symmetrized along both the Ox and Oy axis after each iteration. Additionally, the material volume fraction was constrained to be between $0.3 \leq |S| \leq 0.5$. The initial shape in Figure 4(e) is consisting of a regular “bubble” pattern. The collected values of all the coefficients of the aforementioned shape are included succinctly in Table 2.

$$\begin{array}{c}\boldsymbol{C}^{\text{target}}\\ \left[\begin{array}{ccc|ccc} 0.12 & -0.06 & 0 & \star & 2.3\text{e}^{-3} & 0\\ -0.06 & 0.12 & 0 & 2.3\text{e}^{-3} & \star & 0\\ 0 & 0. & \star & 0 & 0. & \star\\ \hline \star & 2.3\text{e}^{-3} & 0 & 6.3\text{e}^{-4} & \star & 0\\ 2.3\text{e}^{-3} & \star & 0 & \star & 6.3\text{e}^{-4} & 0\\ 0 & 0 & \star & 0 & 0 & \star \end{array}\right]\end{array} \qquad \begin{array}{c}\boldsymbol{C}^{*}\\ \left[\begin{array}{ccc|ccc} 0.097 & -0.033 & 0 & -2.9\text{e}^{-4} & 2.2\text{e}^{-4} & 0\\ -0.033 & 0.098 & 0 & 2.7\text{e}^{-4} & -2.8\text{e}^{-4} & 0\\ 0. & 0. & \star & 0. & 0. & \star\\ \hline \star & 2.7\text{e}^{-4} & 0 & 2.7e^{-4} & \star & 0\\ 2.2e^{-4} & \star & 0 & \star & 2.7e^{-4} & 0\\ 0. & 0. & \star & 0. & 0. & \star \end{array}\right]\end{array}$$

Table 2: Values of the target stiffness tensors and the homogenized tensors for the final form of the microstructure in Figure 9. Only the entries that have numerical values were controlled. The remaining entries were left free.

The convergence history of the cost functional and of the volume constraint displayed in Figure 8(a) shows that the shape gets stabilized in the very first 10 iterations, while the later iteration contributed only to small improvements without bringing the cost functional to less than 4×10^{-3}. Although the gain in the cost functional gets decreased by a factor of 10^3, a remaining gap with respect to the target moduli can be read from Table 2, in particular in the sub-matrix $\boldsymbol{B}$. We conclude that this shape corresponds to a local minima for the objective function, but the shape is not as effective as the one in Table 1. The evolution of material volume fraction displayed in Figure 8(b) features an initial steep decrease down to 0.25, attributed to the initial swelling of the holes, followed by a slower evolution to up to 0.33.

The final shape can be characterized as a “dimpled” sheet structure and looks similar to the designs

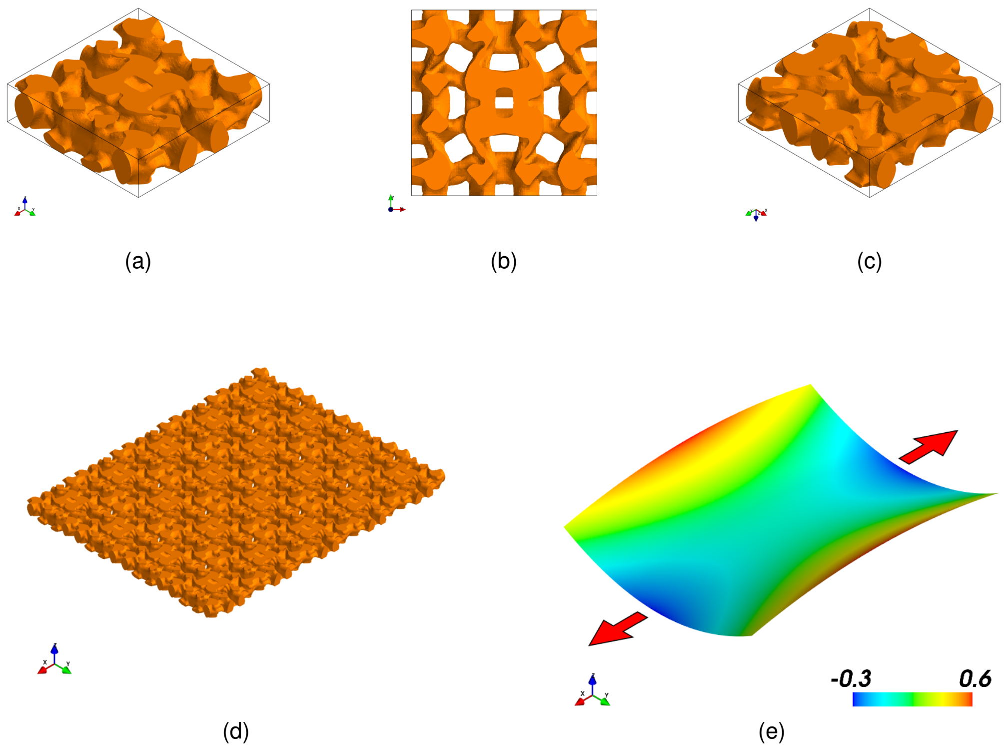

Figure 7: Optimally designed periodic panels accounting for extension-bending coupling effects, with an attained volume fraction of 0.5. Images (a) and (c) show the top and bottom of the periodic cell, while image (b) shows a bird's eye view of the cell. Image (d) shows a 4×5 periodically assembled panel while image (e) shows its macroscopic response assuming the homogeneous equivalent plate model with the coefficients of Table 1 under a uniaxial tensile load up to 10% macroscopic strain. The deformed shape is a saddle. The out-of-plane displacement is plotted as a color map on the deformed equivalent homogeneous panel.

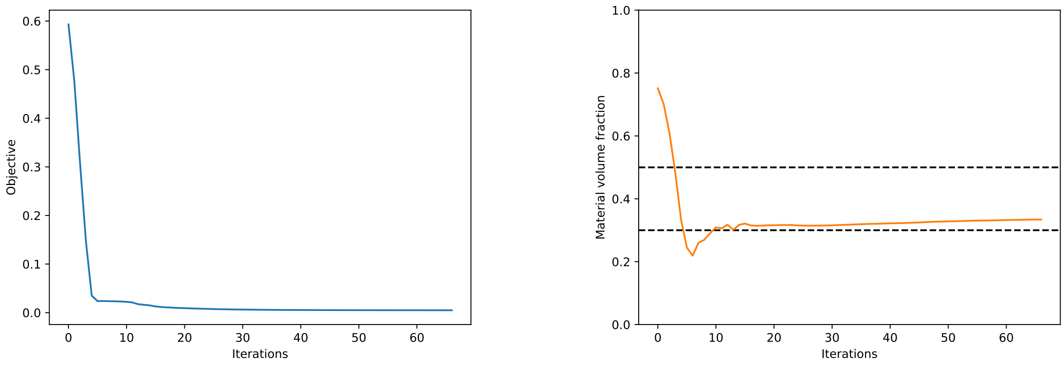

(a) (b)

Figure 8: Evolution of the cost functional (a) and the volume constraint (b) with the number of iterations for the microstructure depicted in Figure 9. After 6 iterations, we seem to have rather stable convergence both for the cost functional and volume constraint. The algorithm stops after 65 iterations, because the time step in the advection equation becomes too small.

imagined in [35]. As prescribed, the final shape features an in-plane auxetic behaviour with a Poisson's ratio of -0.33. The values of B_{1122} and B_{2211} which describe the coupled response between longitudinal in-plane strain and the transverse curvature, as well as the stiff bending behaviour are close to the target value. Moreover, we note that the diagonal coefficient in the Oy direction is much smaller than the coefficient in the Ox direction. This implies that when the panel is loaded in the direction Ox, it will exhibit a positive Gaussian curvature, i.e. the panel with morph into a dome shape. Conversely, when the panels is loaded in the direction Oy, the deformed shape will morph into a cylinder and, hence, will have a Gaussian curvature close to 0.

5.3 Example 3

The targets of the third micro-structure to be optimized are given in Table 3. The material volume fraction, once again, was constrained to be between $0.3 \leq |S| \leq 0.5$. The initial shape, depicted in Figure 4(d), consists of a diagonal pattern of "cone" micro-perforations. The collected values of all the coefficients of the aforementioned shape are succinctly included in Table 3.

$$
\begin{array}{cc}
\boldsymbol{C}^{\text{target}} & \boldsymbol{C}^{*} \\
\left[\begin{array}{ccc|ccc}
0.12 & -0.03 & 0 & \star & 2.3\text{e}^{-3} & 0 \\
-0.03 & 0.12 & 0 & -2.3\text{e}^{-3} & \star & 0 \\
0 & 0. & \star & 0 & 0. & \star \\
\hline
\star & -2.3\text{e}^{-3} & 0 & 6.3\text{e}^{-4} & \star & 0 \\
2.3\text{e}^{-3} & \star & 0 & \star & 6.3\text{e}^{-4} & 0 \\
0 & 0 & \star & 0 & 0 & \star
\end{array}\right]
&
\left[\begin{array}{ccc|ccc}
0.106 & -3\text{e}^{-4} & 0 & 9.5\text{e}^{-3} & 1.8\text{e}^{-4} & 0 \\
-3\text{e}^{-4} & 0.114 & 0 & -8.3\text{e}^{-5} & -7.6\text{e}^{-3} & 0 \\
0. & 0. & \star & 0. & 0. & \star \\
\hline
\star & -8.3\text{e}^{-5} & 0 & 9.4e^{-4} & \star & 0 \\
2.7e^{-4} & \star & 0 & \star & 7.3e^{-4} & 0 \\
0. & 0. & \star & 0. & 0. & \star
\end{array}\right]
\end{array}
$$

Table 3: Values of the target stiffness tensors and the homogenized tensors for the final form of the micro-structure in Figure 11. Only the entries that have numerical values were controlled. The remaining entries were left free.

The convergence history of the cost functional and of the volume constraint displayed in Figure 10(a)

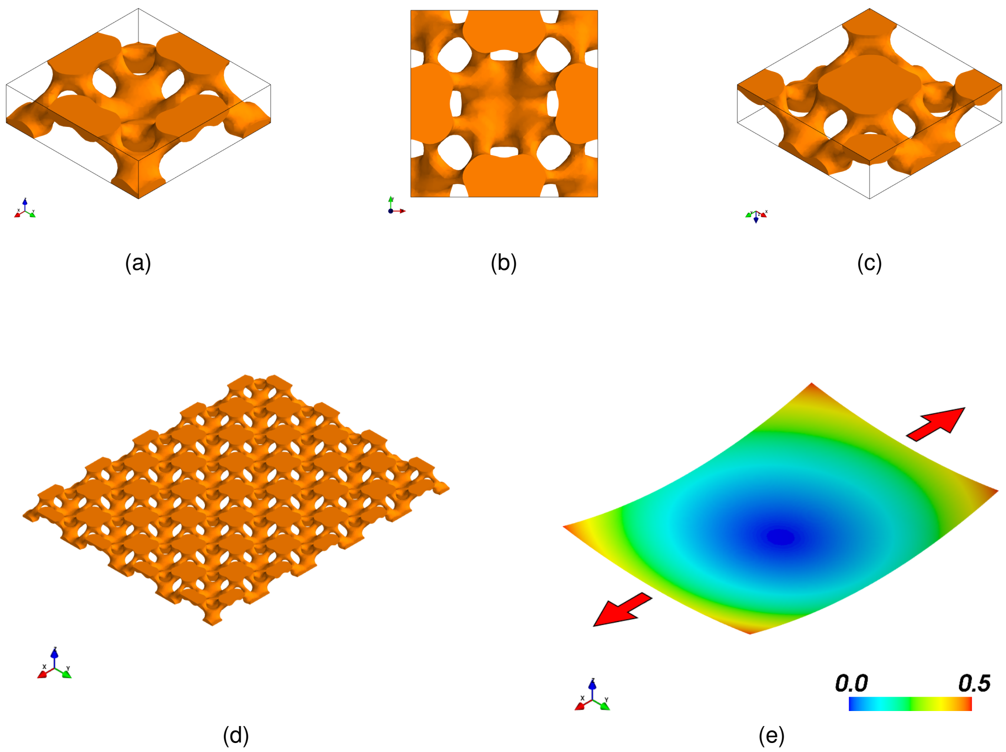

Figure 9: Optimally designed periodic panel resulting in a “dimpled” sheet structure. The attained volume fraction is 33%. Images (a) and (c) show the top and bottom of the periodic cell, while image (b) shows a bird’s eye view of the cell. Image (d) shows a 4×5 periodically assembled panel while image (e) shows its macroscopic response assuming the homogeneous equivalent plate model with the coefficients of Table 2 under a uniaxial tensile load up to 10% macroscopic strain. The deformed shape is a circular dome. The out-of-plane displacement is plotted as a color map on the deformed equivalent homogeneous panel.

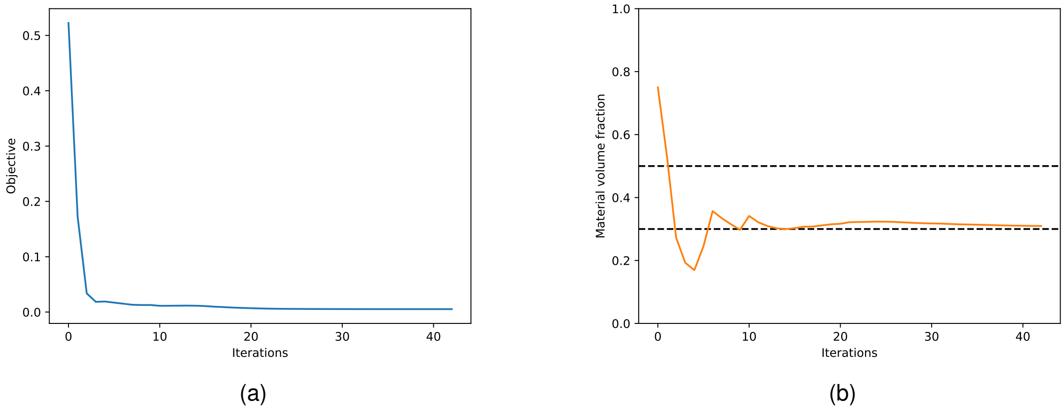

Figure 10: Evolution of the cost functional (a) and the volume constraint (b) for the number of iterations for the microstructure depicted in Figure 11. After 6 iterations, we seem to have rather stable convergence both for the cost functional and volume constraint. The algorithm stops after 43 iterations, because the time step in the advection equation becomes too small.

shows that the shape gets stabilized in the very first 10 iterations, while the later iteration contributed only to small improvements without bringing the cost functional to less than 4×10^{-3}. Although the gain in the cost functional gets decreased by a factor of 10^3, a remaining gap with respect to the target moduli can be read from Table 2, in particular in the block matrix $\boldsymbol{B}$. We conclude that this shape corresponds to a local minima for the objective function, but the shape is not as effective as the one in Table 1. The evolution of material volume fraction displayed in Figure 10(b) features an initial steep decrease down to 0.25, attributed to the initial swelling of the holes, followed by a slower evolution to up to 0.33.

The final shape is similar to the pantograph structures discussed in [27], however, we notice that the vertical beams are on top of the horizontal beams. The micro-structure exhibits a mild auxetic response with an in-plane apparent Poisson's ratio of $\nu^* = -0.25$ but a remaining gap with respect to the target moduli can be read from Table 3.

5.4 Example 4

The targets for the last micro-structure to be optimized are given in Table 4. The material volume fraction, once more, was constrained to be between $0.3 \leq |S| \leq 0.5$. The initial shape, depicted in Figure 4(d), consists of a diagonal pattern of "cone" micro-perforations. The collected values of all the coefficients of the aforementioned shape are succinctly included in Table 4.

The convergence history of the cost functional and of the volume constraint displayed in Figure 12(a) shows that the shape gets stabilized in the very first 10 iterations, while the later iteration contributed only to small improvements without bringing the cost functional to less than 4×10^{-3}. Although the gain in the cost functional gets decreased by a factor of 10^3, a remaining gap with respect to the target moduli can be read from Table 2, in particular in the sub-matrix $\boldsymbol{B}$. We conclude that this shape corresponds to a local minima for the objective function, but the shape is not as effective as the one in Table 1. The evolution of material volume fraction displayed in Figure 12(b) features an initial steep decrease down to 0.15, attributed to the initial swelling of the holes, followed by a and a slower evolution starting from

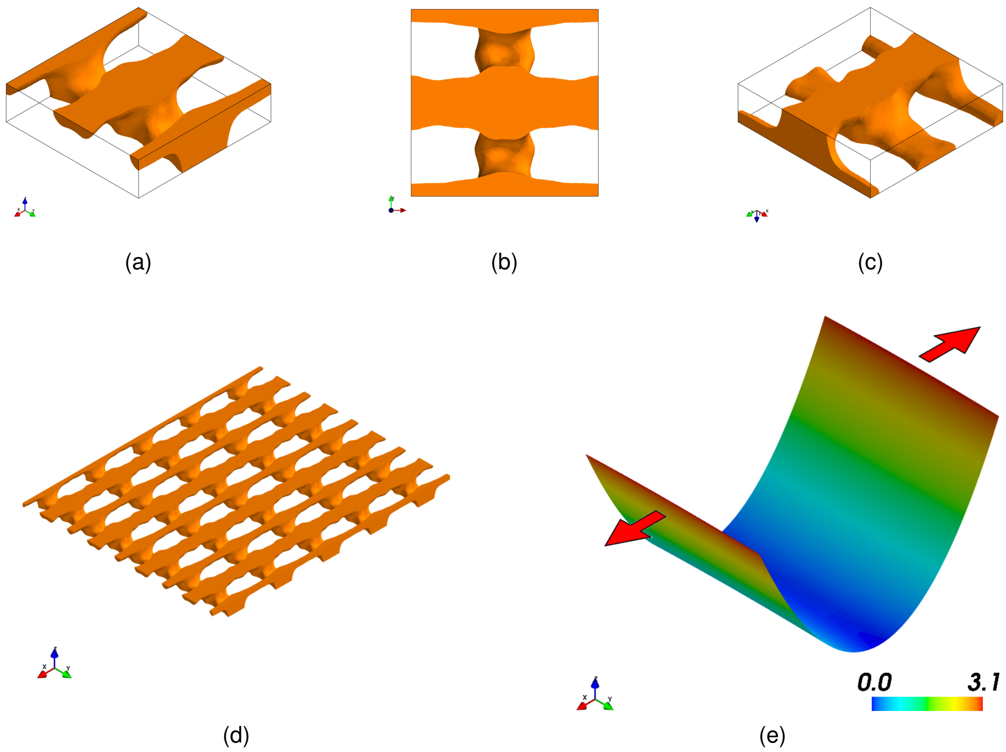

Figure 11: Optimally designed periodic panels accounting for bending-stretch effects mimicking a pantograph structure. The attained volume fraction is 30%, which corresponds to lower bound of the volume interval set. Images (a) and (c) show the top and bottom of the periodic cell, while image (b) shows a bird's eye view of the cell. Image (d) shows a 4×5 periodically assembled panel while image (e) shows its macroscopic response assuming the homogeneous equivalent plate model with the coefficients of Table 3 under a uniaxial tensile load up to 10% macroscopic strain. The deformed shape is a cylinder. The out-of-plane displacement is plotted as a color map on the deformed equivalent homogeneous panel.

$$\boldsymbol{C}^{\text{target}} \qquad\qquad\qquad\qquad \boldsymbol{C}^{*}$$

$$\left[\begin{array}{ccc|ccc} 0.12 & -0.06 & 0 & \star & 2.3\mathrm{e}^{-3} & 0 \\ -0.06 & 0.12 & 0 & 2.3\mathrm{e}^{-3} & \star & 0 \\ 0 & 0. & \star & 0 & 0. & \star \\ \hline \star & 2.3\mathrm{e}^{-3} & 0 & 6.3\mathrm{e}^{-4} & \star & 0 \\ 2.3\mathrm{e}^{-3} & \star & 0 & \star & 6.3\mathrm{e}^{-4} & 0 \\ 0 & 0 & \star & 0 & 0 & \star \end{array}\right] \quad \left[\begin{array}{ccc|ccc} 0.124 & -0.056 & 0 & 3.8\mathrm{e}^{-3} & 1.23\mathrm{e}^{-4} & 0 \\ -0.056 & 0.125 & 0 & -2.2\mathrm{e}^{-4} & 2.97\mathrm{e}^{-3} & 0 \\ 0. & 0. & \star & 0. & 0. & \star \\ \hline \star & -8.3\mathrm{e}^{-5} & 0 & 8.8\mathrm{e}^{-4} & \star & 0 \\ 2.7e^{-4} & \star & 0 & \star & 9.4\mathrm{e}^{-4} & 0 \\ 0. & 0. & \star & 0. & 0. & \star \end{array}\right]$$

Table 4: Values of the target stiffness tensors and the homogenized tensors for the final form of the microstructure in Figure 13. Only the entries that have numerical values were controlled. The remaining entries were left free.

iteration 40 to up to 0.48.

The final shape is of the rotating units type, discussed in [33] (see also the third example of a 2D design in [2]). As prescribed, the resulting structure exhibits a "quadratic" symmetry. The computed effective Poisson's ratio is $\nu^* = -0.45$ and, moreover, the extension bending coupling arises from the fact that

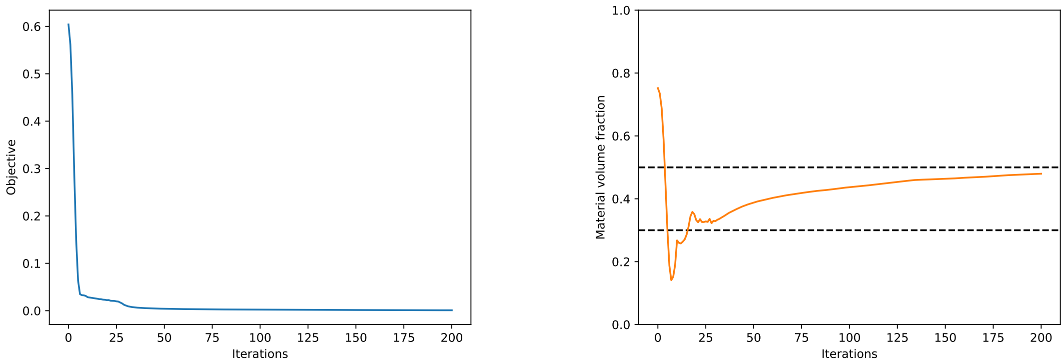

(a) (b)

Figure 12: Evolution of the cost functional (a) and the volume constraint (b) for the number of iterations for the microstructure depicted in Figure 13. After 40 iterations, we seem to have rather stable convergence both for the cost functional and volume constraint. The algorithm stops after 200 iterations.

the structure is asymmetric along its thickness, being bulkier on one side.

6 Conclusion and perspectives

We proposed a method for two-scale topology optimization of micro-structured thin panels with in-plane periodicity. We use inverse homogenization and a level set method coupled with the Hadamard shape derivative to construct plate elastic moduli within the periodic cell in the context of the diffuse inter-phase approach that exhibit certain prescribed macroscopic behaviour for a single material and "void" while simultaneously accounting for bending-stretching effects. By controlling the micro-structure of the panel, we simultaneously controlled the in-plane, out-of-plane and their coupled behaviour and in doing so we designed panels with an out-of-plane response that results in either a dome shaped structure or a saddle shaped structure under the action of in-plane loading. By and large, these building blocks can be leveraged in systematic design of shape morphing structures. Moreover, the obtained shapes are directly realizable through additive manufacturing techniques.

References

[1] N. Aage, E. Andreassen, and B. S. Lazarov. "Topology optimization using PETSc: An easy-to-use, fully parallel, open source topology optimization framework". In: *Structural and Multidisciplinary Optimization* 51.3 (2014), pp. 565–572. DOI: 10.1007/s00158-014-1157-0.

[2] F. Agnelli, A. Constantinescu, and G. Nika. "Design and testing of 3D-printed micro-architectured polymer materials exhibiting a negative Poisson's ratio". In: *Continuum Mechanics and Thermodynamics* 32.2 (Mar. 2020), pp. 433–449. DOI: 10.1007/s00161-019-00851-6.

[3] F. Agnelli, M. Tricarico, and A. Constantinescu. "Shape-shifting panel from 3D printed undulated ribbon lattice". In: *Extreme Mechanics Letters* 42 (Jan. 2021), p. 101089. DOI: 10.1016/j.eml.2020.101089.

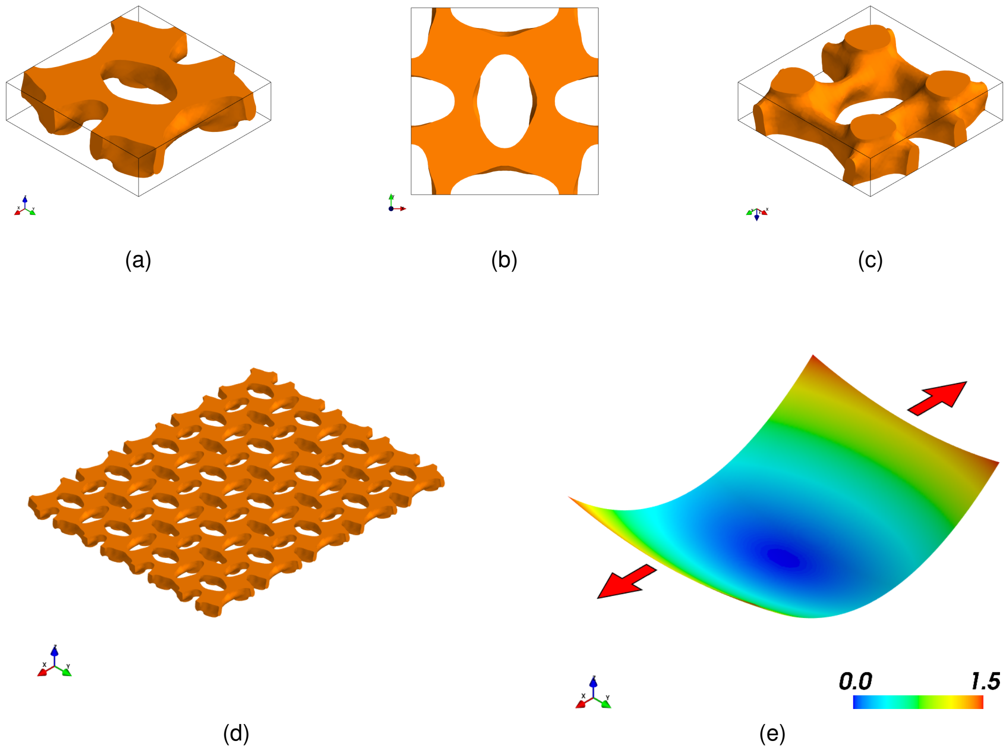

Figure 13: Optimally designed periodic panels accounting for bending-stretch effects. The attained volume fraction is 0.48, which corresponds to lower bound of the volume interval set. Images (a) and (c) show the top and bottom of the periodic cell, while image (b) shows a bird's eye view of the cell. Image (d) shows a 4×5 periodically assembled panel while image (e) shows its macroscopic response assuming the homogeneous equivalent plate model with the coefficients of Table 4 under a uniaxial tensile load up to 10% macroscopic strain. The deformed shape is an ellipsoidal dome. The out-of-plane displacement is plotted as a color map on the deformed equivalent homogeneous panel.

[4] G. Allaire. *Shape Optimization by the Homogenization Method*. Springer New York, 2002. ISBN: 1441929428. DOI: 10.1007/978-1-4684-9286-6.

[5] G. Allaire et al. “Multi-phase structural optimization via a level set method”. English. In: *ESAIM: Control, Optimisation and Calculus of Variations* 20.2 (Mar. 2014), pp. 576–611. DOI: 10.1051/cocv/2013076.

[6] G. Allaire, F. Jouve, and A.-M. Toader. “Structural optimization using sensitivity analysis and a level-set method”. English. In: *Journal of Computational Physics* 194.1 (Feb. 2004), pp. 363–393. DOI: 10.1016/j.jcp.2003.09.032.

[7] G. Allaire. *Conception optimale de structures*. Springer Berlin Heidelberg, 2007. ISBN: 978-3-540-36856-4. DOI: 10.1007/978-3-540-36856-4.

[8] M. N. Andersen, F. Wang, and O. Sigmund. “On the competition for ultimately stiff and strong architected materials”. In: *Materials & Design* 198 (Jan. 2021), p. 109356. DOI: 10.1016/j.matdes.2020.109356.

[9] E. Andreassen, B. S. Lazarov, and O. Sigmund. “Design of manufacturable 3D extremal elastic microstructure”. In: *Mechanics of Materials* 69.1 (Feb. 2014), pp. 1–10. DOI: 10.1016/j.mechmat.2013.09.018.

[10] N. S. Bakhvalov and G. Panasenko. *Homogenisation: Averaging Processes in Periodic Media*. Springer Netherlands, 2011. ISBN: 9401075069. DOI: 10.1007/978-94-009-2247-1.

[11] K.-J. Bathe, E. Dvorkin, and L. W. Ho. “Our discrete-Kirchhoff and isoparametric shell elements for nonlinear analysis—An assessment”. In: *Computers & Structures* 16.1-4 (Jan. 1983), pp. 89–98. DOI: 10.1016/0045-7949(83)90150-5.

[12] A. A. Bauhofer et al. “Harnessing photochemical shrinkage in direct laser writing for shape morphing of polymer sheets”. English. In: *Advanced Materials* 29.42 (Sept. 2017), p. 1703024. DOI: 10.1002/adma.201703024.

[13] M. P. Bendsøe and N. Kikuchi. “Generating optimal topologies in structural design using a homogenization method”. English. In: *Computer Methods in Applied Mechanics and Engineering* 71.2 (Nov. 1988), pp. 197–224. DOI: 10.1016/0045-7825(88)90086-2.

[14] M. P. Bendsøe and O. Sigmund. *Topology Optimization. Theory, Methods and Applications*. Springer Berlin Heidelberg, 2004. ISBN: 978-3-662-05086-6. DOI: 10.1007/978-3-662-05086-6.

[15] A. Bensoussan, J.-L. Lions, and G. Papanicolaou. *Asymptotic Analysis for Periodic Structures*. Amsterdam New York New York: North-Holland Pub. Co. Sole distributors for the U.S.A. and Canada, Elsevier North-Holland, 1978. ISBN: 9780080875262. DOI: 10.1090/chel/374.

[16] D. Bertsekas. *Constrained Optimization and Lagrange Multiplier Methods*. Belmont, Mass: Athena Scientific, 1982. ISBN: 1886529043. DOI: 10.1016/c2013-0-10366-2.

[17] O. R. Bilal et al. “Intrinsically polar elastic metamaterials”. English. In: *Advanced Materials* 29.26 (May 2017), p. 1700540. DOI: 10.1002/adma.201700540.

[18] T. Bückmann et al. “Tailored 3D mechanical metamaterials made by dip-in direct-laser-writing optical lithography”. English. In: *Advanced Materials* 24.20 (Apr. 2012), pp. 2710–2714. DOI: 10.1002/adma.201200584.

[19] T. T. C. Bui, C. Dapogny, and P. Frey. “An accurate anisotropic adaptation method for solving the level set advection equation”. English. In: *International Journal for Numerical Methods in Fluids* 70.7 (Nov. 2011), pp. 899–922. DOI: 10.1002/fld.2730.

[20] D. Caillerie and J.-C. Nedelec. “Thin elastic and periodic plates”. English. In: *Mathematical Methods in the Applied Sciences* 6.1 (Jan. 1984), pp. 159–191. DOI: 10.1002/mma.1670060112.

[21] J. Céa. “Conception optimale ou identification de formes, calcul rapide de la dérivée directionnelle de la fonction coût”. Francais. In: *ESAIM: Mathematical Modelling and Numerical Analysis* 20.3 (1986), pp. 371–402. DOI: 10.1051/m2an/1986200303711.

[22] T. Chen et al. “Harnessing bistability for directional propulsion of soft, untethered robots”. In: *Proceedings of the National Academy of Sciences* 115.22 (May 2018), pp. 5698–5702. DOI: 10.1073/pnas.1800386115.

[23] D. Cioranescu and P. Donato. *An introduction to homogenization*. Oxford New York: Oxford University Press, 1999. ISBN: 0198565542.

[24] A. Clausen et al. “Topology optimized architectures with programmable Poisson’s ratio over large deformations”. English. In: *Advanced Materials* 27.37 (Aug. 2015), pp. 5523–5527. DOI: 10.1002/adma.201502485.

[25] C. Dapogny and P. Frey. “Computation of the signed distance function to a discrete contour on adapted triangulation”. In: *Calcolo* 49.3 (Jan. 2012), pp. 193–219. DOI: 10.1007/s10092-011-0051-z.

[26] M. C. Delfour and J.-P. Zolésio. *Shapes and geometries: metrics, analysis, differential calculus, and optimization*. Society for Industrial and Applied Mathematics, 2011. DOI: 10.1137/1.9780898719826.

[27] F. Dell’Isola et al. “Advances in pantographic structures: design, manufacturing, models, experiments and image analyses”. In: *Continuum Mechanics and Thermodynamics* 31.4 (June 2019), pp. 1231–1282. DOI: 10.1007/s00161-019-00806-x.

[28] H. A. Eschenauer and N. Olhoff. “Topology optimization of continuum structures: A review*”. In: *Applied Mechanics Reviews* 54.4 (July 2001), pp. 331–390. DOI: 10.1115/1.1388075.

[29] F. Fraternali and A. Amendola. “Mechanical modeling of innovative metamaterials alternating pentamode lattices and confinement plates”. In: *Journal of the Mechanics and Physics of Solids* 99 (Feb. 2017), pp. 259–271. DOI: 10.1016/j.jmps.2016.11.010.

[30] T. Frenzel, M. Kadic, and M. Wegener. “Three-dimensional mechanical metamaterials with a twist”. English. In: *Science* 358.6366 (Nov. 2017), pp. 1072–1074. DOI: 10.1126/science.aao4640.

[31] L. V. Gibiansky and A. V. Cherkaev. “Design of Composite Plates of Extremal Rigidity”. In: *Topics in the Mathematical Modelling of Composite Materials*. Ed. by A. V. Cherkaev and R. V. Kohn. Springer International Publishing, 1997, pp. 95–137. DOI: 10.1007/978-3-319-97184-1_5.

[32] L. J. Gibson et al. “The Mechanics of Two-Dimensional Cellular Materials”. In: *Proceedings of the Royal Society A: Mathematical, Physical and Engineering Sciences* 382.1782 (July 1982), pp. 25–42. DOI: 10.1098/rspa.1982.0087.

[33] J. N. Grima et al. “Auxetic behaviour from rotating semi-rigid units”. In: *Physica Status Solidi B* 244.3 (Mar. 2007), pp. 866–882. DOI: 10.1002/pssb.200572706.

[34] R. Guseinov, E. Miguel, and B. Bickel. “CurveUps : Shaping Objects from Flat Plates with Tension-Actuated Curvature”. In: *ACM Transactions on Graphics* 36.4 (July 2017), pp. 1–12. DOI: 10.1145/3072959.3073709.

[35] B. Hassani, S. M. Tavakkoli, and H. Ghasemnejad. “Simultaneous shape and topology optimization of shell structures”. In: *Structural and Multidisciplinary Optimization* 48.1 (2013), pp. 221–233. DOI: 10.1007/s00158-013-0894-9.

[36] A. Henrot and M. Pierre. *Variation et optimisation de formes*. Springer Berlin Heidelberg, 2005. DOI: 10.1007/3-540-37689-5.

[37] G. Imbalzano et al. “A numerical study of auxetic composite panels under blast loadings”. English. In: *Composite Structures* 135 (Jan. 2016), pp. 339–352. DOI: 10.1016/j.compstruct.2015.09.038.

[38] Z. X. Khoo et al. “3D printing of smart materials: A review on recent progresses in 4D printing”. In: *Virtual and Physical Prototyping* 10.3 (July 2015), pp. 103–122. DOI: 10.1080/17452759.2015.1097054.

[39] R. V. Kohn and M. Vogelius. “A new model for thin plates with rapidly varying thickness”. English. In: *International Journal of Solids and Structures* 20.4 (1984), pp. 333–350. DOI: 10.1016/0020-7683(84)90044-1.

[40] A. Kotikian et al. “Untethered soft robotic matter with passive control of shape morphing and propulsion”. English. In: *Science Robotics* 4.33 (Aug. 2019), eaax7044. DOI: 10.1126/scirobotics.aax7044.

[41] S. Krödel et al. “Stress relaxation in polymeric microlattice materials”. English. In: *Materials and Design* 130 (Sept. 2017), pp. 433–441. DOI: 10.1016/j.matdes.2017.05.060.

[42] T. Lewinski and J. J. Telega. *Plates, Laminates and Shells*. World Scientific, 2000. DOI: 10.1142/3539.

[43] F. López Jimnez and N. Triantafyllidis. “Buckling of rectangular and hexagonal honeycomb under combined axial compression and transverse shear”. In: *International Journal of Solids and Structures* 50.24 (2013), pp. 3934–3946. DOI: 10.1016/j.ijsolstr.2013.08.001.

[44] L. Malomo et al. “FlexMaps: Computational Design of Flat Flexible Shells for Shaping 3D Objects”. In: *ACM Transactions on Graphics* 37.6 (Dec. 2018), pp. 1–14. DOI: 10.1145/3272127.3275076.

[45] C. C. Mei and B. Vernescu. *Homogenization Methods for Multiscale Mechanics*. World Scientific, Sept. 2010. ISBN: 978-981-4282-44-4. DOI: 10.1142/7427.

[46] G. W. Milton. *The Theory of Composites*. Cambridge University Press, 2002. ISBN: 0-521-78125-6. DOI: 10.1017/cbo9780511613357.

[47] G. W. Milton and A. V. Cherkaev. “Which elasticity tensors are realizable?” English. In: *Journal of Engineering Materials and Technology* 117.4 (Oct. 1995), pp. 483–493. DOI: 10.1115/1.2804743.

[48] G. W. Milton and R. V. Kohn. “Variational bounds on the effective moduli of anisotropic composites”. English. In: *Journal of the Mechanics and Physics of Solids* 36.6 (Jan. 1988), pp. 597–629. DOI: 10.1016/0022-5096(88)90001-4.

[49] F. Murat and J. Simon. “Etude de problemes d’optimal design”. In: *Lecture Notes in Computer Science*. Springer Berlin Heidelberg, 1976, pp. 54–62. DOI: 10.1007/3-540-07623-9_279.

[50] G. Nika and A. Constantinescu. “Design of multi-layer materials using inverse homogenization and a level set method”. English. In: *Computer Methods in Applied Mechanics and Engineering* 346 (Apr. 2019), pp. 388–409. DOI: 10.1016/j.cma.2018.11.029.

[51] S. Nishi et al. “Two-scale topology optimization for composite plates with in-plane periodicity”. In: *International Journal for Numerical Methods in Engineering* 113.8 (2017), pp. 1164–1188. DOI: 10.1002/nme.5545.

[52] J. Nocedal and S. J. Wright. *Numerical Optimization*. Springer New York, 2006. DOI: 10.1007/978-0-387-40065-5.

[53] K. Oliver, A. Seddon, and R. S. Trask. “Morphing in nature and beyond: a review of natural and synthetic shape-changing materials and mechanisms”. In: *Journal of Materials Science* 51.24 (Aug. 2016), pp. 10663–10689. DOI: 10.1007/s10853-016-0295-8.

[54] S. J. Osher and J. A. Sethian. “Fronts propagating with curvature-dependent speed: algorithms based on Hamilton-Jacobi formulations”. English. In: *Journal of Computational Physics* 79.1 (Nov. 1988), pp. 12–49. DOI: 10.1016/0021-9991(88)90002-2.

[55] O. Pironneau. *Optimal Shape Design for Elliptic Systems*. Springer Berlin Heidelberg, 1984. DOI: 10.1007/978-3-642-87722-3.

[56] A. Rafsanjani and D. Pasini. “Bistable auxetic mechanical metamaterials inspired by ancient geometric motifs”. In: *Extreme Mechanics Letters* 9 (Dec. 2016), pp. 291–296. DOI: 10.1016/j.eml.2016.09.001.

[57] K. Sab and A. Lebe. *Homogenization of Heterogeneous Thin and Thick Plates*. John Wiley & Sons, Inc., Oct. 2015. DOI: 10.1002/9781119005247.

[58] E. Sanchez-Palencia. *Non-Homogeneous Media and Vibration Theory*. English. Springer Berlin Heidelberg, 1980. ISBN: 978-3-540-10000-3. DOI: 10.1007/3-540-10000-8.

[59] O. Sigmund. “Materials with prescribed constitutive parameters: an inverse homogenization problem”. In: *International Journal of Solids and Structures* 31.17 (Sept. 1994), pp. 2313–2329. DOI: 10.1016/0020-7683(94)90154-6.

[60] O. Sigmund. “On the usefulness of non-gradient approaches in topology optimization”. In: *Structural and Multidisciplinary Optimization* 43.5 (Mar. 2011), pp. 589–596. DOI: 10.1007/s00158-011-0638-7.

[61] D. G. Talaslidis and I. I. Sous. “A discrete kirchhoff triangular element for the analysis of thin stiffened shells”. In: *Computers & Structures* 43.4 (May 1992), pp. 663–674. DOI: 10.1016/0045-7949(92)90507-v.

[62] N. Triantafyllidis and M. W. Schraad. “Onset of failure in aluminum honeycombs under general in-plane loading”. In: *Journal of the Mechanics and Physics of Solids* 46.6 (1998), pp. 1089–1124. DOI: 10.1016/s0022-5096(97)00060-4.

[63] P. Vogiatzis et al. “Topology optimization of multi-material negative Poisson’s ratio metamaterials using a reconciled level set method”. English. In: *Computer-Aided Design* 83 (Feb. 2017), pp. 15–32. DOI: 10.1016/j.cad.2016.09.009.

[64] F. Wang. “Systematic design of 3D auxetic lattice materials with programmable Poisson’s ratio for finite strains”. In: *Journal of the Mechanics and Physics of Solids* 114 (May 2018), pp. 303–318. DOI: 10.1016/j.jmps.2018.01.013.

[65] F. Wang, O. Sigmund, and J. S. Jensen. “Design of materials with prescribed nonlinear properties”. In: *Journal of the Mechanics and Physics of Solids* 69 (Sept. 2014), pp. 156–174. DOI: 10.1016/j.jmps.2014.05.003.

[66] X. Wang, Y. Mei, and M. Y. Wang. “Level-set method for design of multi-phase elastic and thermoelastic materials”. English. In: *International Journal of Mechanics and Materials in Design* 1.3 (Sept. 2004), pp. 213–239. DOI: 10.1007/s10999-005-0221-8.

[67] Y. Wang et al. “Topological shape optimization of microstructural metamaterials using a level set method”. In: *Computational Materials Science* 87 (May 2014), pp. 178–186. DOI: 10.1016/j.commatsci.2014.02.006.

[68] X. F. Xu and P. Qiao. “Homogenized elastic properties of honeycomb sandwich with skin effect”. In: *International Journal of Solids and Structures* 39.8 (Apr. 2002), pp. 2153–2188. DOI: 10.1016/s0020-7683(02)00111-7.

[69] H. X. Zhu and N. J. Mills. “The in-plane non-linear compression of regular honeycombs”. In: *International Journal of Solids and Structures* 37.13 (Mar. 2000), pp. 1931–1949. DOI: 10.1016/s0020-7683(98)00324-2.

A Shape propagation analysis

A.1 Shape derivative in the smoothed-interface context

Using the method of Ca, discussed in [21], for the calculation of the shape derivative of the objective function, we formulate the Lagrangian function $\mathcal{L} : W^{1,\infty}(Y,\mathbb{R}^3) \times \mathcal{V} \times \mathcal{V} \times \mathcal{V} \times \mathcal{V} \to \mathbb{R}$ as follows:

$$\begin{aligned}
&\mathcal{L}\left(S, \boldsymbol{\xi}^{\gamma\delta}, \Xi, \boldsymbol{\zeta}^{\gamma\delta}, \boldsymbol{Z}\right) \\
&\quad = \frac{1}{2}\left\|\boldsymbol{A}^* - \boldsymbol{A}^{\text{target}}\right\|^2_{\eta_A} + \frac{1}{2}\left\|\boldsymbol{B}^* - \boldsymbol{B}^{\text{target}}\right\|^2_{\eta_B} + \frac{1}{2}\left\|\boldsymbol{D}^* - \boldsymbol{D}^{\text{target}}\right\|^2_{\eta_D} \\
&\quad + \int_Y \boldsymbol{C}(\boldsymbol{y}) : \left(\boldsymbol{E}^{\gamma\delta} + \boldsymbol{\varepsilon}_{\boldsymbol{y}}(\boldsymbol{\xi}^{\gamma\delta})\right) : \boldsymbol{\varepsilon}_{\boldsymbol{y}}(\Xi)\, d\boldsymbol{y} \\
&\quad + \int_Y \boldsymbol{C}(\boldsymbol{y}) : \left(\boldsymbol{X}^{\alpha\beta} + \boldsymbol{\varepsilon}_{\boldsymbol{y}}(\boldsymbol{\zeta}^{\alpha\beta})\right) : \boldsymbol{\varepsilon}_{\boldsymbol{y}}(\boldsymbol{Z})\, d\boldsymbol{y}.
\end{aligned} \tag{27}$$

Here, Ξ, $\boldsymbol{Z}$ are intended as the Lagrange multipliers associated to the enforcement of the state equations. $\boldsymbol{\xi}^{\gamma\delta}$, Ξ, $\boldsymbol{\zeta}^{\gamma\delta}$ and $\boldsymbol{Z}$ are vector-valued functions defined in Y, which do not depend on S. As usual, the stationarity of the Lagrangian provides the optimality conditions for the minimization problem.

Direct problem. Differentiating $\mathcal{L}$ in (27) with respect to Ξ in the direction of a test function $\boldsymbol{\varphi} \in H^1(Y,\mathbb{R}^3)$ gives:

$$\left\langle \frac{\partial \mathcal{L}}{\partial \Xi} \mid \boldsymbol{\varphi} \right\rangle = \int_Y \boldsymbol{C}(\boldsymbol{y}) : \left(\boldsymbol{E}^{\gamma\delta} + \boldsymbol{\varepsilon}_{\boldsymbol{y}}(\boldsymbol{\xi}^{\gamma\delta})\right) : \boldsymbol{\varepsilon}_{\boldsymbol{y}}(\boldsymbol{\varphi})\, d\boldsymbol{y},$$

Upon setting the above equation equal to zero, we recover the variational formulation of first state equation (7). Similarly, differentiating $\mathcal{L}$ (27) with respect to $\boldsymbol{Z}$ in the direction of a test function $\boldsymbol{\varphi} \in H^1(Y,\mathbb{R}^3)$ gives:

$$\left\langle \frac{\partial \mathcal{L}}{\partial \boldsymbol{Z}} \mid \boldsymbol{\varphi} \right\rangle = \int_Y \boldsymbol{C}(\boldsymbol{y}) : \left(\boldsymbol{X}^{\alpha\beta} + \boldsymbol{\varepsilon}_{\boldsymbol{y}}(\boldsymbol{\zeta}^{\alpha\beta})\right) : \boldsymbol{\varepsilon}_{\boldsymbol{y}}(\boldsymbol{\varphi})\, d\boldsymbol{y},$$

Upon setting the above equation equal to zero, we recover the variational formulation of second state equation (8).

Adjoint problem. The partial derivative of $\mathcal{L}$ in (27) with respect to $\boldsymbol{\xi}^{\gamma\delta}$ in the direction of a test function $\boldsymbol{\psi} \in H^1(Y,\mathbb{R}^3)$ results in:

$$\begin{aligned}
\left\langle \frac{\partial \mathcal{L}}{\partial \boldsymbol{\xi}^{\gamma\delta}} \mid \boldsymbol{\psi} \right\rangle &= \frac{r}{|Y|}\left\|\boldsymbol{A}^* - \boldsymbol{A}^{\text{target}}\right\|_{\eta_A} \int_Y \boldsymbol{C}(\boldsymbol{y}) : \boldsymbol{\varepsilon}_{\boldsymbol{y}}(\boldsymbol{\psi}) : \left(\boldsymbol{E}^{\gamma\delta} + \boldsymbol{\varepsilon}_{\boldsymbol{y}}(\boldsymbol{\xi}^{\gamma\delta})\right) d\boldsymbol{y} \\
&+ \frac{r}{|Y|}\left\|\boldsymbol{B}^* - \boldsymbol{B}^{\text{target}}\right\|_{\eta_B} \int_Y \boldsymbol{C}(\boldsymbol{y}) : \boldsymbol{\varepsilon}_{\boldsymbol{y}}(\boldsymbol{\psi}) : \left(\boldsymbol{X}^{\gamma\delta} + \boldsymbol{\varepsilon}_{\boldsymbol{y}}(\boldsymbol{\zeta}^{\gamma\delta})\right) d\boldsymbol{y} \\
&+ \int_Y \boldsymbol{C}(\boldsymbol{y}) : \boldsymbol{\varepsilon}_{\boldsymbol{y}}(\boldsymbol{\psi}) : \boldsymbol{\varepsilon}_{\boldsymbol{y}}(\Xi)\, d\boldsymbol{y}.
\end{aligned}$$

The integral over Y on the first two lines is equal to 0 from the state equations (7) and (8). Moreover, if we choose $\boldsymbol{\psi} = \boldsymbol{\Xi}$ and using the positive definiteness of $\boldsymbol{C}$ as well as the Y-periodicity of $\boldsymbol{\Xi}$, we obtain that the solution of the adjoint state is identically zero, $\boldsymbol{\Xi} = \mathbf{0}$. Similarly, the partial derivative of $\mathcal{L}$ with respect to $\boldsymbol{\zeta}^{\gamma\delta}$ in the direction of a test function $\boldsymbol{\psi} \in H^1(Y, \mathbb{R}^3)$ results in:

$$\begin{aligned}\left\langle \frac{\partial \mathcal{L}}{\partial \boldsymbol{\zeta}^{\gamma\delta}} \mid \boldsymbol{\psi} \right\rangle &= \frac{r}{|Y|} \left\| \boldsymbol{B}^* - \boldsymbol{B}^{\text{target}} \right\|_{\eta_B} \int_Y \boldsymbol{C}(\boldsymbol{y}) : \left(\boldsymbol{E}^{\gamma\delta} + \boldsymbol{\varepsilon_y}(\boldsymbol{\xi}^{\gamma\delta}) \right) : \boldsymbol{\varepsilon_y}(\boldsymbol{\psi})\, d\boldsymbol{y} \\ &+ \frac{r}{|Y|} \left\| \boldsymbol{D}^* - \boldsymbol{D}^{\text{target}} \right\|_{\eta_D} \int_Y \boldsymbol{C}(\boldsymbol{y}) : \left(\boldsymbol{X}^{\gamma\delta} + \boldsymbol{\varepsilon_y}(\boldsymbol{\zeta}^{\gamma\delta}) \right) : \boldsymbol{\varepsilon_y}(\boldsymbol{\psi})\, d\boldsymbol{y} \\ &+ \int_Y \boldsymbol{C}(\boldsymbol{y}) : \boldsymbol{\varepsilon_y}(\boldsymbol{\psi}) : \boldsymbol{\varepsilon_y}(\boldsymbol{Z})\, d\boldsymbol{y}.\end{aligned}$$

The integral over Y on the first two lines is equal to 0 from the state equations (7) and (8). Moreover, if we choose $\boldsymbol{\psi} = \boldsymbol{Z}$ and using the positive definiteness of $\boldsymbol{C}$ as well as the Y-periodicity of $\boldsymbol{Z}$, we obtain that the solution of the adjoint state is identically zero, $\boldsymbol{Z} = \mathbf{0}$.

Shape derivative. Deforming the interface Γ in the direction of a smooth vector field $\boldsymbol{\theta}$, the shape derivative of the objective function is found to be the shape derivative of the Lagrangian at the optimal point:

$$\mathcal{J}'(S)(\boldsymbol{\theta}) = \left\langle \frac{\partial \mathcal{L}}{\partial S} \left(S, \boldsymbol{w}^{\gamma\delta}, \mathbf{0}, \boldsymbol{p}^{\gamma\delta}, \mathbf{0} \right) \mid \boldsymbol{\theta} \right\rangle. \tag{28}$$

Thus:

$$\begin{aligned}\mathcal{J}'(S)(\boldsymbol{\theta}) =& \frac{r}{|Y|} \left\| \boldsymbol{A}^*(d_S) - \boldsymbol{A}^{\text{target}} \right\|_{\eta_A} \\ & \quad \int_Y d_S'(\boldsymbol{\theta})\, \boldsymbol{C}'(d_S) : \left(\boldsymbol{E}^{\gamma\delta} + \boldsymbol{\varepsilon_y}(\boldsymbol{w}^{\gamma\delta}) \right) : \left(\boldsymbol{E}^{\alpha\beta} + \boldsymbol{\varepsilon_y}(\boldsymbol{w}^{\alpha\beta}) \right) d\boldsymbol{y} \\ &+ \frac{r}{|Y|} \left\| \boldsymbol{B}^*(d_S) - \boldsymbol{B}^{\text{target}} \right\|_{\eta_B} \\ & \quad \int_Y d_S'(\boldsymbol{\theta})\, \boldsymbol{C}'(d_S) : \left(\boldsymbol{E}^{\gamma\delta} + \boldsymbol{\varepsilon_y}(\boldsymbol{w}^{\gamma\delta}) \right) : \left(\boldsymbol{X}^{\alpha\beta} + \boldsymbol{\varepsilon_y}(\boldsymbol{p}^{\alpha\beta}) \right) d\boldsymbol{y} \\ &+ \frac{r}{|Y|} \left\| \boldsymbol{D}^*(d_S) - \boldsymbol{D}^{\text{target}} \right\|_{\eta_D} \\ & \quad \int_Y d_S'(\boldsymbol{\theta})\, \boldsymbol{C}'(d_S) : \left(\boldsymbol{X}^{\gamma\delta} + \boldsymbol{\varepsilon_y}(\boldsymbol{p}^{\gamma\delta}) \right) : \left(\boldsymbol{X}^{\alpha\beta} + \boldsymbol{\varepsilon_y}(\boldsymbol{p}^{\alpha\beta}) \right) d\boldsymbol{y}\end{aligned}$$

Moreover, as presented in Proposition 2.5 and then Proposition 2.9 from [5], the shape derivative can be expressed as follows:

$$\begin{aligned}\mathcal{J}'(S)(\boldsymbol{\theta}) =& \frac{r}{|Y|} \left\| \boldsymbol{A}^*(d_S) - \boldsymbol{A}^{\text{target}} \right\|_{\eta_A} \int_{\Gamma^S} -\boldsymbol{\theta} \cdot \boldsymbol{n}\, f_A(\boldsymbol{s})\, d\boldsymbol{s} \\ &+ \frac{r}{|Y|} \left\| \boldsymbol{B}^*(d_S) - \boldsymbol{B}^{\text{target}} \right\|_{\eta_B} \int_{\Gamma^S} -\boldsymbol{\theta} \cdot \boldsymbol{n}\, f_B(\boldsymbol{s})\, d\boldsymbol{s} \\ &+ \frac{r}{|Y|} \left\| \boldsymbol{D}^*(d_S) - \boldsymbol{D}^{\text{target}} \right\|_{\eta_D} \int_{\Gamma^S} -\boldsymbol{\theta} \cdot \boldsymbol{n}\, f_D(\boldsymbol{s})\, d\boldsymbol{s},\end{aligned} \tag{29}$$

where:

$$\begin{cases} f_A(\boldsymbol{s}) = \displaystyle\int_{\text{ray}_{\partial S} \cap Y} \left[\prod_{i=1}^{2} 1 + d_S(\boldsymbol{z})\kappa_i(\boldsymbol{s})\right] \mathcal{H}'_e(d_S) \\ \qquad\qquad \left(\boldsymbol{C}^{\bar{S}} - \boldsymbol{C}^{S}\right) : \left(\boldsymbol{E}^{\gamma\delta} + \boldsymbol{\varepsilon}_{\boldsymbol{z}}(\boldsymbol{w}^{\gamma\delta})\right) : \left(\boldsymbol{E}^{\alpha\beta} + \boldsymbol{\varepsilon}_{\boldsymbol{z}}(\boldsymbol{w}^{\alpha\beta})\right) d\boldsymbol{z} \\ f_B(\boldsymbol{s}) = \displaystyle\int_{\text{ray}_{\partial S} \cap Y} \left[\prod_{i=1}^{2} 1 + d_S(\boldsymbol{z})\kappa_i(\boldsymbol{s})\right] \mathcal{H}'_e(d_S) \\ \qquad\qquad \left(\boldsymbol{C}^{\bar{S}} - \boldsymbol{C}^{S}\right) : \left(\boldsymbol{E}^{\gamma\delta} + \boldsymbol{\varepsilon}_{\boldsymbol{z}}(\boldsymbol{w}^{\gamma\delta})\right) : \left(\boldsymbol{X}^{\alpha\beta} + \boldsymbol{\varepsilon}_{\boldsymbol{z}}(\boldsymbol{p}^{\alpha\beta})\right) d\boldsymbol{z} \\ f_D(\boldsymbol{s}) = \displaystyle\int_{\text{ray}_{\partial S} \cap Y} \left[\prod_{i=1}^{2} 1 + d_S(\boldsymbol{z})\kappa_i(\boldsymbol{s})\right] \mathcal{H}'_e(d_S) \\ \qquad\qquad \left(\boldsymbol{C}^{\bar{S}} - \boldsymbol{C}^{S}\right) : \left(\boldsymbol{X}^{\gamma\delta} + \boldsymbol{\varepsilon}_{\boldsymbol{z}}(\boldsymbol{p}^{\gamma\delta})\right) : \left(\boldsymbol{X}^{\alpha\beta} + \boldsymbol{\varepsilon}_{\boldsymbol{z}}(\boldsymbol{p}^{\alpha\beta})\right) d\boldsymbol{z} \end{cases}$$

A.2 Approximate formula for the shape derivative

Although formula (29) is satisfying from a mathematical point of view, its numerical evaluation is not completely straightforward. There are two delicate issues. First, one has to compute the principal curvatures $\kappa_i(\boldsymbol{s})$ for any point $\boldsymbol{s} \in \Gamma$ on the interface. Second, one has to perform a 1-d integration along the rays of the energy-like quantity. This is a classical task in the level set framework but, still, it is of interest to devise a simpler approximate formula for the shape derivative.

Following the ideas developed in [5], a first approximate formula is to assume that the interface is roughly plane, namely to assume that the principal curvatures $\kappa_i(\boldsymbol{s})$ vanish. In such a case we obtain a "Jacobian-free" approximate shape derivative. This gives a new expression for f_A, f_B and f_D:

$$\begin{cases} f_A(\boldsymbol{s}) = \displaystyle\int_{\mathrm{ray}_{\partial S} \cap Y} \mathcal{H}'_e(d_S) \left(\boldsymbol{C}^{\bar{S}} - \boldsymbol{C}^{S}\right) : \left(\boldsymbol{E}^{\gamma\delta} + \boldsymbol{\varepsilon}_{\boldsymbol{z}}(\boldsymbol{w}^{\gamma\delta})\right) : \left(\boldsymbol{E}^{\alpha\beta} + \boldsymbol{\varepsilon}_{\boldsymbol{z}}(\boldsymbol{w}^{\alpha\beta})\right) d\boldsymbol{z} \\ f_B(\boldsymbol{s}) = \displaystyle\int_{\mathrm{ray}_{\partial S} \cap Y} \mathcal{H}'_e(d_S) \left(\boldsymbol{C}^{\bar{S}} - \boldsymbol{C}^{S}\right) : \left(\boldsymbol{E}^{\gamma\delta} + \boldsymbol{\varepsilon}_{\boldsymbol{z}}(\boldsymbol{w}^{\gamma\delta})\right) : \left(\boldsymbol{X}^{\alpha\beta} + \boldsymbol{\varepsilon}_{\boldsymbol{z}}(\boldsymbol{p}^{\alpha\beta})\right) d\boldsymbol{z} \\ f_D(\boldsymbol{s}) = \displaystyle\int_{\mathrm{ray}_{\partial S} \cap Y} \mathcal{H}'_e(d_S) \left(\boldsymbol{C}^{\bar{S}} - \boldsymbol{C}^{S}\right) : \left(\boldsymbol{X}^{\gamma\delta} + \boldsymbol{\varepsilon}_{\boldsymbol{z}}(\boldsymbol{p}^{\gamma\delta})\right) : \left(\boldsymbol{X}^{\alpha\beta} + \boldsymbol{\varepsilon}_{\boldsymbol{z}}(\boldsymbol{p}^{\alpha\beta})\right) d\boldsymbol{z} \end{cases}$$

A second approximate formula is obtained when the smoothing parameter e is small. Note that, since the support of the function h_e is of size $2e$, the integral in formula (29) is confined to a tubular neighbourhood of Γ of width $2e$. Therefore, if e is small, one may assume that the functions depending on $\boldsymbol{z}$ are constant along each ray, equal to their value at $\boldsymbol{y} \in \Gamma$. In other words, for small e we assume:

$$\boldsymbol{\varepsilon}_{\boldsymbol{z}} \approx \boldsymbol{\varepsilon}_{\boldsymbol{s}}, \qquad d_S(\boldsymbol{z}) \approx d_S(\boldsymbol{s}) = 0, \tag{30}$$

which yields the approximate formulas, for $\boldsymbol{y} \in \Gamma^S$,

$$\begin{cases} f_A(\boldsymbol{s}) = \left(\boldsymbol{C}^{\bar{S}} - \boldsymbol{C}^S\right) : \left(\boldsymbol{E}^{\gamma\delta} + \boldsymbol{\varepsilon_s}(\boldsymbol{w}^{\gamma\delta})\right) : \left(\boldsymbol{E}^{\alpha\beta} + \boldsymbol{\varepsilon_s}(\boldsymbol{w}^{\alpha\beta})\right) \displaystyle\int_{\mathrm{ray}_{\partial S} \cap Y} \mathcal{H}'_e(d_S)\, d\boldsymbol{z} \\ f_B(\boldsymbol{s}) = \left(\boldsymbol{C}^{\bar{S}} - \boldsymbol{C}^S\right) : \left(\boldsymbol{E}^{\gamma\delta} + \boldsymbol{\varepsilon_s}(\boldsymbol{w}^{\gamma\delta})\right) : \left(\boldsymbol{X}^{\alpha\beta} + \boldsymbol{\varepsilon_s}(\boldsymbol{p}^{\alpha\beta})\right) \displaystyle\int_{\mathrm{ray}_{\partial S} \cap Y} \mathcal{H}'_e(d_S) d\boldsymbol{z} \\ f_D(\boldsymbol{s}) = \left(\boldsymbol{C}^{\bar{S}} - \boldsymbol{C}^S\right) : \left(\boldsymbol{X}^{\gamma\delta} + \boldsymbol{\varepsilon_s}(\boldsymbol{p}^{\gamma\delta})\right) : \left(\boldsymbol{X}^{\alpha\beta} + \boldsymbol{\varepsilon_s}(\boldsymbol{p}^{\alpha\beta})\right) \displaystyle\int_{\mathrm{ray}_{\partial S} \cap Y} \mathcal{H}'_e(d_S) d\boldsymbol{z} \end{cases}$$

Furthermore, most rays have a length larger than $2e$ so that

$$\int_{\mathrm{ray}_{\partial S} \cap Y} \mathcal{H}'_e(d_\omega)\, d\boldsymbol{z} + \int_{\mathrm{ray}_{\partial S} \cap Y} \mathcal{H}'_e(d_\omega)\, d\boldsymbol{z} = \mathcal{H}_e(e) - \mathcal{H}_e(-e) = 1. \tag{31}$$

In turn, the shape derivative in (29) can be approximated by:

$$\begin{aligned} \mathcal{J}'(S)(\boldsymbol{\theta}) =& \frac{r}{|Y|} \left\| \boldsymbol{A}^*(d_S) - \boldsymbol{A}^{\mathrm{target}} \right\|_{\eta_A} \int_{\Gamma^S} -\boldsymbol{\theta} \cdot \boldsymbol{n} \\ & \left(\boldsymbol{C}^{\bar{S}} - \boldsymbol{C}^S\right) : \left(\boldsymbol{E}^{\gamma\delta} + \boldsymbol{\varepsilon_s}(\boldsymbol{w}^{\gamma\delta})\right) : \left(\boldsymbol{E}^{\alpha\beta} + \boldsymbol{\varepsilon_s}(\boldsymbol{w}^{\alpha\beta})\right) d\boldsymbol{s} \\ & + \frac{r}{|Y|} \left\| \boldsymbol{B}^*(d_S) - \boldsymbol{B}^{\mathrm{target}} \right\|_{\eta_B} \int_{\Gamma^S} -\boldsymbol{\theta} \cdot \boldsymbol{n} \\ & \left(\boldsymbol{C}^{\bar{S}} - \boldsymbol{C}^S\right) : \left(\boldsymbol{E}^{\gamma\delta} + \boldsymbol{\varepsilon_s}(\boldsymbol{w}^{\gamma\delta})\right) : \left(\boldsymbol{X}^{\alpha\beta} + \boldsymbol{\varepsilon_s}(\boldsymbol{p}^{\alpha\beta})\right) d\boldsymbol{s} \\ & + \frac{r}{|Y|} \left\| \boldsymbol{D}^*(d_S) - \boldsymbol{D}^{\mathrm{target}} \right\|_{\eta_D} \int_{\Gamma^S} -\boldsymbol{\theta} \cdot \boldsymbol{n} \\ & \left(\boldsymbol{C}^{\bar{S}} - \boldsymbol{C}^S\right) : \left(\boldsymbol{X}^{\gamma\delta} + \boldsymbol{\varepsilon_z}(\boldsymbol{p}^{\gamma\delta})\right) : \left(\boldsymbol{X}^{\alpha\beta} + \boldsymbol{\varepsilon_z}(\boldsymbol{p}^{\alpha\beta})\right) d\boldsymbol{s} \end{aligned} \tag{32}$$

Numerical results performed in [5] reveal that the latter simplification (32), which we shall refer to as the approximate shape derivative, works very well in practice for problems of compliance minimization. Formula (32) is also used by Wang et al. in their numerical simulations [66].

B Volume constraint

The volume constraint is enforced using an augmented Lagrangian approach to enforce a two-sided inequality constraints [16], [52, Chapter 17]. Hence, the optimisation problem (11) is a constraint-free minimization of a (Lagrangian-like) weighted sum of the cost functional $\mathcal{J}(S)$ and the constraint $\mathcal{P}(S)$ that reads:

$$\begin{aligned} & \inf \left(\mathcal{J}(S) + \mathcal{P}(S)\right), \\ & \mathcal{P}(S, \lambda, \mu) = \min_{f_m \le |S| - \upsilon \le f_M} \left(\lambda\, \upsilon + \frac{\mu}{2} |\upsilon|^2\right), \end{aligned} \tag{33}$$

where λ and μ are the Lagrange multipliers for the volume constraint.

At the iteration k, a straightforward calculation shows that the minimum above is attained at the point υ^k given by:

$$\upsilon^k = \begin{cases} |S| - f_M & \text{if } \lambda^k + \mu^k \left(|S| - f_M\right) > 0 \\ |S| - f_m & \text{if } \lambda^k + \mu^k \left(|S| - f_m\right) < 0 \\ -\lambda^k/\mu^k & \text{otherwise} \end{cases} \tag{34}$$

and $\mathcal{P}$ is given by:

$$\mathcal{P}(S) = \begin{cases} \lambda^k \left(|S| - f_M\right) + \dfrac{\mu^k}{2} |\,|S| - f_M|^2 & \text{if } \lambda^k + \mu^k \left(|S| - f_M\right) > 0 \\ \lambda^k \left(|S| - f_m\right) + \dfrac{\mu^k}{2} |\,|S| - f_m|^2 & \text{if } \lambda^k + \mu^k \left(|S| - f_m\right) < 0 \\ -(\lambda^k)^2/2\mu^k & \text{otherwise} \end{cases} \tag{35}$$

Deforming the interface Γ in the direction of a smooth vector field $\boldsymbol{\theta}$, the shape derivative of the constraint function $\mathcal{P}(S)$ under the approximation of thin smooth inter-phase reads:

$$\mathcal{P}'(S)(\boldsymbol{\theta}) = \begin{cases} \left[\lambda^k + \left(|S| - f_M\right)\mu^k\right] \displaystyle\int_{\Gamma_S} -\boldsymbol{\theta}\cdot\boldsymbol{n}\,d\boldsymbol{s} & \text{if } \lambda^k + \mu^k \left(|S| - f_M\right) > 0 \\ \left[\lambda^k + \left(|S| - f_m\right)\mu^k\right] \displaystyle\int_{\Gamma_S} -\boldsymbol{\theta}\cdot\boldsymbol{n}\,d\boldsymbol{s} & \text{if } \lambda^k + \mu^k \left(|S| - f_m\right) < 0 \\ \boldsymbol{0} & \text{otherwise} \end{cases} \tag{36}$$

The developments to obtain the above equation are identical to the ones performed for $\mathcal{J}(S)$.

The conclusion from the preceding analysis is that a method of multipliers for problem consists of sequential minimizations of the form, which do not involve the variables υ. The (first-order) multiplier iteration is given by:

$$\lambda_{k+1} = \begin{cases} \lambda^k + \mu^k \left(f(S) - f_M\right) & \text{if } \lambda^k + \mu^k \left(f(S) - f_M\right) > 0 \\ \lambda^k + \mu^k \left(f(S) - f_m\right) & \text{if } \lambda^k + \mu^k \left(f(S) - f_m\right) < 0 \\ 0 & \text{otherwise} \end{cases} \tag{37}$$

The last aspect consists in updating the penalty parameters μ every 10 iterations as follows:

$$\mu^{k+10} = 2\mu^k \tag{38}$$

C Constitutive behaviour of laminate plate as a route for prescribing targets

The choice of a target plate tensor may seem a difficult task a priori. The prescribed stiffness coefficients should not compromise the positive definiteness, and should remain bounded imposed by the rule of mixture (e.g. the Voigt-Reuss bounds). Yet, to the best of our knowledge, the clear definition of elastic bounds in the context of thin plates has not been explored, and is beyond the scope of the present work.

We rather address this aspect by studying the laminate plate, a sub-category of elastic plate with periodic pattern. This simpler framework permits to rapidly construct achievable target tensors analytically. In the sequel, we recall the expressions of $\boldsymbol{A}$, $\boldsymbol{B}$, $\boldsymbol{D}$ in the context of the classical laminate plate theory (CPLT) [57], and illustrate the construction of a target through an simple case which is used in the numerical examples (section 5).

Note that a limiting case for a homogeneous thin plate theory should be the Kirchhoff-Love plate equations. Let us consider the definition of $\boldsymbol{N}$ as a sum of integrals in each layer:

$$\boldsymbol{N} = \sum_{k=1}^{n} \int_{h_k}^{h_{k+1}} \boldsymbol{\sigma}\, dx_3$$

Introducing the constitutive behaviour layer by layer and using the generalized strain components gives:

$$\boldsymbol{N} = \sum_{k=1}^{n} \int_{h_k}^{h_{k+1}} \boldsymbol{C} : (\boldsymbol{\varepsilon}(\boldsymbol{U}) + x_3\, \boldsymbol{\chi}(U_3))\ dx_3$$

Since the generalized strains do not depend upon x_3, one can write:

$$\begin{aligned}\boldsymbol{N} &= \left[\sum_{k=1}^{n} \int_{h_k}^{h_{k+1}} \boldsymbol{C}\, dx_3\right] : \boldsymbol{\varepsilon}(\boldsymbol{U}) + \left[\sum_{k=1}^{n} \int_{h_k}^{h_{k+1}} x_3\, \boldsymbol{C}\, dx_3\right] : \boldsymbol{\chi}(U_3) \\ &= \boldsymbol{A} : \boldsymbol{\varepsilon}(\boldsymbol{U}) + \boldsymbol{B} : \boldsymbol{\chi}(U_3)\end{aligned} \tag{39}$$

Following the same reasoning for M we can write:

$$\begin{aligned}\boldsymbol{M} &= \left[\sum_{k=1}^{n} \int_{h_k}^{h_{k+1}} x_3\, \boldsymbol{C}\, dx_3\right] : \boldsymbol{\varepsilon}(\boldsymbol{U}) + \left[\sum_{k=1}^{n} \int_{h_k}^{h_{k+1}} x_3^2\, \boldsymbol{C}\, dx_3\right] : \boldsymbol{\chi}(U_3) \\ &= \boldsymbol{B} : \boldsymbol{\varepsilon}(\boldsymbol{U}) + \boldsymbol{D} : \boldsymbol{\chi}(U_3)\end{aligned} \tag{40}$$

Thus, the plate constitutive law is:

$$\begin{bmatrix}\boldsymbol{N}\\ \boldsymbol{M}\end{bmatrix} = \begin{bmatrix}\boldsymbol{A} & \boldsymbol{B}\\ \boldsymbol{B} & \boldsymbol{D}\end{bmatrix} : \begin{bmatrix}\boldsymbol{\varepsilon}\\ \boldsymbol{\chi}\end{bmatrix}$$

Like in the thin plates with periodic micro-structure, the general laminate plate model induces an extension-bending coupling in the most general case. It is a consequence of the heterogeneous or anisotropic properties of the panel (variations between each ply). To illustrate this effect, let us consider a simple bi-phase composite panels, i.e. composed by two superposed plates that are perfectly glued at their interface. It is assumed in this example that the upper plate is stiffer than the lower one in the direction $(O, \boldsymbol{e}_1)$. Under a tensile loading in the direction $(O, \boldsymbol{e}_1)$, not only the plate is stretched in the direction $(O, \boldsymbol{e}_1)$, it also undergoes an out of plane curvature (hence a coupled response).

The main difference between the laminate plate theory and the panel with periodic micro-structure lies in the fact that $\boldsymbol{B}$ is symmetric in the case of laminates, but not necessarily in the case of periodic plates.

Example. Let us consider a bi-phase laminate plate of thickness $2h$, composed of isotropic plies of equal thickness. The material in the upper ply S_p is described by Young's modulus $E_p = 0.4608\,\mathrm{MPa}$ and Poisson's ratio is $\nu_p = -0.2$, whereas the material in lower ply S_m features a Young's modulus $E_m = 0.1728\,\mathrm{MPa}$ and Poisson's ratio is $\nu_m = -0.8$. The resulting laminate plate stiffness tensor, computed analytically from eqs. (39) and (40), reads:

$$\left[\begin{array}{ccc|ccc} 0.12 & -0.06 & 0 & 0. & 2.3\mathrm{e}^{-3} & 0 \\ -0.06 & 0.12 & 0 & 2.3\mathrm{e}^{-3} & 0. & 0 \\ 0 & 0. & \star & 0 & 0. & \star \\ \hline \star & 2.3\mathrm{e}^{-3} & 0 & 6.3\mathrm{e}^{-4} & \star & 0 \\ 2.3\mathrm{e}^{-3} & \star & 0 & \star & 6.3\mathrm{e}^{-4} & 0 \\ 0 & 0 & \star & 0 & 0 & \star \end{array}\right] \tag{41}$$

The process can be extended to laminate with n ply, where each ply is orthotropic.

DOI 10.20347/WIAS.PREPRINT.2873